SMHI

-20   -18   -16   -14   -12   -10   -8   -6   -4 (dB)

Time Series Analysis of SAR Sea Ice Backscatter Variability and its Dependence on Weather Conditions

Maria Lundin

Front cover: Temporal mean image of 17 calibrated ERS-1 SAR images, showing an area of 26×59 km of the northernmost part of Bothnian Bay. High values represent rough land and ice areas, while low values show smoother ice.

Time Series Analysis of SAR Sea Ice Backscatter Variability and its Dependence on Weather Conditions

Maria Lundin

Report Summary / Rapportsammanfattning

Author (s)/Författare

Maria Lundin

Title (and Subtitle/Titel

Time Series Analysis of SAR Sea Ice Backscatter Variability and its Dependence on Weather Conditions

Abstract/Sammandrag

Synthetic Aperture Radar (SAR) is an active satellite sensor, recording satellite images by measuring the echo of transmitted microwave pulses. Compared to other satellite sensors, SAR records high resolution data and since it is an active sensor, it is independent of what time of the day it measures. SAR is also independent of clouds, however not totally weather independent. The images change appearance depending on weather conditions.

This thesis describes the variability of the backscatter ccoefficient and the texture of sea ice in Synthetic Aperture Radar (SAR) images and its dependency on air temperature, air humidity, air water content and precipitation. A time series of radiometric calibrated ERS-1 SAR Low Resolution Images (LRI) from the Bothnian Bay have been studied.

It is important to further develop the interpretation of SAR images and increase the understanding of the effects of various weather conditions, in order to increase the usefulness of the images. SAR images are for example currently used operationally in the Swedish and Finnish ice breaking services.

From spatial variations in the temporal variability of texture and backscatter coefficient, five ice classes have been defined in the time series of LRI. In a case study, a correlation between rising air temperature and a decrease in backscatter coefficient is shown. Also, an Empirical Orthogonal Function (EOF) analysis shows that the air temperature and air water content are the dominating parameters affecting the backscattered signal from the investigated surfaces.

Key words/sök-, nyckelord

SAR, ERS-1, ice classification, EOF, calibration, satellite images, backscatter coefficient, Bothnian Bay

Report available from/Rapporten kan köpas från:

SMHI
S-601 76 NORRKÖPING
Sweden

Contents

1 Introduction

Synthetic Aperture Radar (SAR) is an active satellite[1] sensor, recording satellite images by measuring the echo of transmitted microwave pulses. SAR images are for example currently used operationally in the Swedish and Finnish ice-breaking services in the Baltic sea, in order to give an overview of the ice situation. Compared to other satellite sensors, SAR records high resolution data and since it is an active sensor, it is independent of what time of the day it measures. SAR is also independent of clouds, however not totally weather independent. The images change appearance depending on weather conditions.
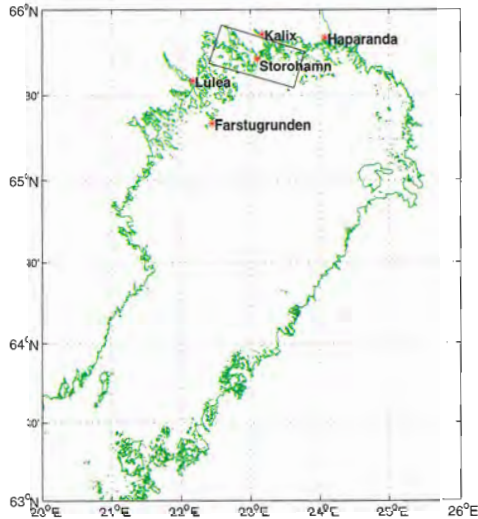

Figure 1: Bothnian Bay in the northern part of the Baltic sea. The square represents the area covered by the SAR images. Figure 2 shows the area in more detail. Storöhamn and Farstugrunden are weather stations providing data used in this study.

---

[1]SAR sensors can also be air-borne.

The objective of this thesis is to study images of first year sea ice and quantify their dependency on weather parameters. For this, a time series of SAR images, measured by the satellite ERS-1, covering a part of Bothnian Bay in the Baltic Sea, have been studied. The weather parameters used, are air temperature, air humidity, air water content and precipitation. This study aims to increase the usefulness of SAR images by developing the interpretation of the images. Future use of SAR data includes modeling, climate studies and monitoring.

First, a short introduction to microwave radars and the SAR system is presented in Section 2. In Section 3, the theory of backscatter, especially for snow and ice, is discussed. The weather and ice conditions of the area and time of the images are presented in Section 4. Section 5 contains a description of the image and meteorological data used for the analysis. How the images are calibrated is described in Section 6 and Section 7 introduces the theory of Principal Components (PC) and their connection to Empirical Orthogonal Functions (EOF).

The analysis of the images and the results from this analysis is discussed in Section 8. The last two sections contain summary and conclusions and a discussion of future work on the subject matter.

2 Synthetic Aperture Radar (SAR)

In this section, the concept of the active microwave system SAR will be sorted out. First follows a brief introduction to active microwave sensors in general. Then the SAR system characteristics, for example range and azimuth resolution and speckle phenomenon, are discussed.
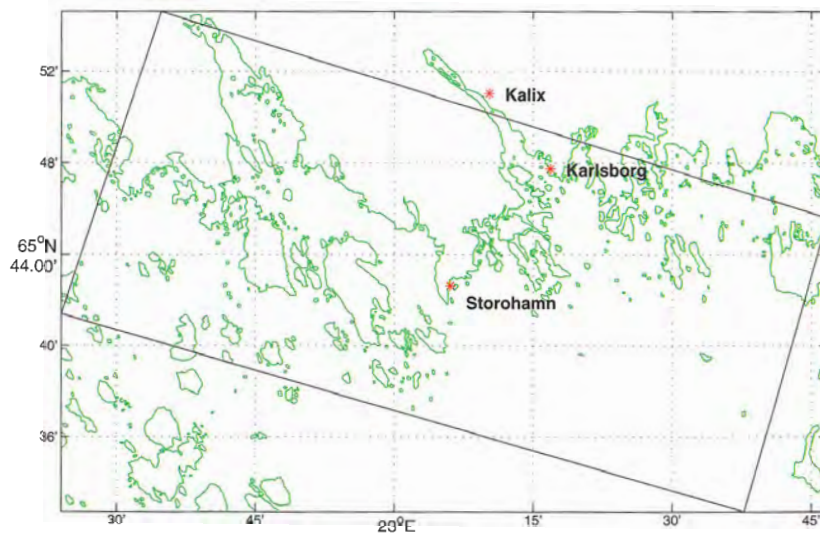
2

Figure 2: The square represents the area covered by the SAR images.

Finally the ERS-1 SAR system is presented. The symbols, equations and data in this section are mainly taken from [Rob95] and [Ela88].

2.1 Active Microwave Sensors in General

A radar emits pulses of microwave radiation. Due to the relative long wave length the microwaves are able to penetrate through clouds in the atmosphere. The microwave sensor detects the returned signal, which carries information about the surface and the intervening path. The information content depends on type of sensor, the properties of the returned signal and the viewing angle of the sensor. This will be discussed further in Section 3.

Radars can be divided into three classes:

- *Altimeter radar*, radar using specular reflection, which will be explained in Section 3.1. It measures the height relative to the satellite. The timing and the pulse form of the returned signal is recorded.

- *Scatterometer* and *Imaging radar*, radars which views obliquely. On these radars the magnitude of the returned signal is recorded. The scatterometer records the average power of the returned pulse. This is good for global coverage, since it averages roughness over a wide area and measures for example surface wind with very coarse resolution, 16-50 km. Imaging radar records the full time history of the returned pulse. There are two different kinds of imaging radars: *SLAR* (Side-looking airborne radar) and *SAR* (Synthetic Aperture Radar). SLAR is a real aperture radar used for oil spill detection and ship reconnaissance by several Coast Guard organizations. It has high resolution in range direction, 10m-20m, and angular dependent resolution in azimuth direction. SAR has very high

3

resolution in both range and azimuth direction. Range and azimuth direction are explained in Figure 4.

- *Weather radar, Marine (navigation) radar and H.F.(High Frequency) shore-based radar*, radar using grazing or near horizontal incidence angle.

In the next two sections, the SAR system is described in more detail.

2.2 SAR (Synthetic Aperture Radar) Principles

SAR is a complex system characterised by high resolution leading to high data rate. Due to the synthesised aperture, the ground system needs computationally intensive processing to recover an image from the raw data. This sections describes the method used to achieve the high resolution with a SAR system.

2.2.1 Range Resolution

Since the time of the returned signal corresponds to a particular range, SAR does not look nadir. That would result in getting two echoes at the same time. The range resolution depends on how precisely this time can be measured, and how short the pulse length is. If all energy is sent at the same time in a very short pulse, it is no question about which part of the signal that was sent first. The problem is that a single pulse, short enough to give accurate range resolution and strong enough to be measurable after scattering at the surface, would require far too much power. However, if the pulse is long, there must be an ability to distinguish the first part of the pulse from the last part, in order to get satisfying resolution. The solution is to use a longer,

frequency modulated pulse, a so called *chirped* pulse, see Figure 3. Using a chirped pulse, the instantaneously emitted power can be low, although the total emitted energy is high. Furthermore, a frequency delay filter can demodulate the emitted pulse to a short spike, which will give sufficient range resolution.

2.2.2 Azimuth Resolution

For a normal aperture radar, the range resolution is much finer than the azimuth. The azimuth resolution is dependent on the width of the beam. A feature is easier to distinguish with a narrow focused beam than with a wide beam, that covers many features. The beam width, β depends on the wavelength of the radar, λ_{radar} and the aperture of the antenna, D_{radar} by the following relation:

$$\beta = \frac{\lambda_{radar}}{D_{radar}} \qquad (1)$$

The symbols β and D_{radar} are marked in Figure 4. Equation 1 implies that a large antenna is required to achieve high resolution in the azimuth direction. This can be illustrated by squeezing a water hose; the more narrow opening the wider beam. The following equation is valid:

$$r = \frac{\lambda_{radar} R}{D_{radar}} \qquad (2)$$

where r is the resolution on the ground at a range R, from the satellite. The shorter the distance between target and satellite, the more narrow becomes the beam leading to higher resolution. SLAR uses a narrow beam while SAR synthesises a narrow beam by signal processing, see Figure 5.

In order to improve the azimuth resolution, the antenna aperture must be made longer in the

Figure 3: A chirped pulse. The pulse is emitted during time ΔT. A signal from near range comes back first, at time A. The last signal comes back from far range at time B. The smallest interval between A and B that can be distinguished is ΔT. With a chirped signal, a shorter time lap than ΔT can be distinguished.

Figure 4: The radar beam. The range resolution is much finer than the azimuth resolution for a normal aperture radar.

Figure 5: Synthesised narrow beam. A wide beam produces an image where the points furthest away are blur. At point P_1 SAR sends out a pulse toward target G for the first time. At point P_2 it sends out another pulse and at P_3 the last pulse that reaches G. In the data processing stage the signals from target G are added. That gives $P_3 - P_1 = D_{SAR}$ where D_{SAR} is the length of the synthetic aperture. The smaller the aperture is, the wider becomes the beam and the longer G will be illuminated by the beam and there will be more information from G to add.

Figure 6: Doppler shift. Because of the Doppler shift in the frequency in the return signal, produced when the satellite moves with constant velocity, the signal from G can be distinguished from other targets on the ground.

azimuth direction. On the ground this can be done by synthesising a long antenna from a line of point antennae, operating simultaneously. In space the same principle is applied, except that the long antenna is synthesised by operating the same short antenna sequentially, at a large number of locations along the orbit track, see Figure 5. To achieve this the returned signal must be recorded in greater detail, and the elapsed time since the emission must be preserved with great accuracy. The resolution, r_{SAR}, based on the synthesised aperture is

$$r_{SAR} = \frac{\lambda_{radar} R}{2 D_{SAR}} \qquad (3)$$
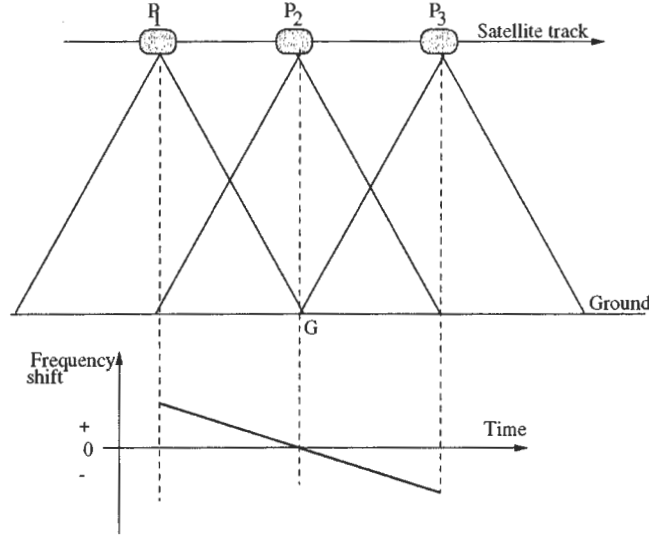
where D_{SAR} is the synthesised aperture, i.e. the distance where G in Figure 5 is within the field of view. If the earth curvature is neglected then $D_{SAR} = r$, see Equation 2. Equations 2 and 3 give

$$r_{SAR} = \frac{\lambda_{radar} R}{2r} = \frac{D_{radar}}{2} \qquad (4)$$

It shows the interesting outcome that a more narrow real aperture gives a better resolution with SAR. However, the aperture can not be too small, since there are some various demands that must be fulfilled. A typical length of the synthesised antenna is 800 m, corresponding to a physical antenna of 10 m.

For a real aperture antenna, only one pulse is transmitted, received and displayed as a single line. For SAR each target will produce a lot of return pulses. To identify where each returning pulse comes from in the illuminated area, the Doppler shift is used. Doppler shift is the changes in frequency when the satellite moves forward, see Figure 6. When processing the data all targets are assumed to be stationary. Due to the Doppler shift this leads to errors when a tar-

get is moving in azimuth direction. As an example, if a train is running towards the satellite in azimuth direction, the train seems to be nearer the satellite than it really is. This leads to a displacement in the SAR image.

To achieve high resolution in azimuth direction the SAR sensor synthesises a long antenna by moving forward, illuminating the same target many times. The received signal, in form of pulses, are stored and added in the right order. This creates the synthetic antenna. The images are built up from the signal time delay and the Doppler shift of the returning signal.

2.2.3 Speckle

Thousands of pulses are emitted over a few seconds. The image is formed by coherently summing the instantaneous amplitudes of the returned pulses within every single resolution element. Since the path to the antenna can differ by several wavelengths for waves from different targets within the resolution cell, the individual returns come back in different phases, meaning varying amplitudes. Adding up all the returns from the individual scatters, Figure 7, each pixel results in a random spikiness, speckle or fading, overlaying the true image. Speckle is a property of backscatter and not a calibration problem. It gives the SAR images their somewhat grainy appearance. Due to the speckle, a single pixel has little significance.

By averaging the SAR images over a certain number of *looks*, the speckle decreases. The number of looks is the number of samples which have been averaged in order to reduce speckle. The number of looks is a common parameter for describing the quality of SAR images. The method is called *multi-looking* and is used at expense of a degradation in spatial resolution. Av-

Figure 7: Vectorial summation of the returns from individual scatters within one resolution element. ϕ is the phase of the signal and R is the resultant. Speckle is defined as interference between the different scattering elements.

eraging can be done in the SAR processing step. There are several techniques for multi-looking.

2.3 The ERS-1 SAR

ERS-1, the first European Remote Sensing Satellite, was launched in July 1991. It was put in stand-by mode in June 1996 but can still be reactivated as back-up for its successor ERS-2. ERS-1 has a sun-synchronous, near polar orbit with a mean altitude of 785 km. The inclination of an orbit is the angle between the plane of the orbit and the equatorial plane. The inclination of ERS-1 is 98.9° and the orbiting period is 100 min. During the period of the images analysed in this thesis, ERS-1 had a 3-day cycle. It means that the satellite was back in the same track every third day.

Among other instruments, ERS-1 has an Active Microwave Instrument, AMI, which consists of a Wind Scatterometer and a Synthetic Aperture Radar, SAR. The Wind Scatterometer uses three antennae to generate sea surface wind speed and direction measurements. SAR uses one antenna which operates in two different modes, wave mode and image mode. The wave mode produces length and direction measurements of ocean waves over 5×5 km. The image mode measures over a wider swath, looking to the right of the satellite. The images that are analysed in this thesis are produced by image mode. SAR image mode needs a lot of power and memory and can therefore only be active for a maximum of 12 min per orbit as it is dependent on solar energy. Due to the high data rate and no storing possibilities on board, SAR can only measure within the reception zone of a ground station. Nowadays, there are enough ground stations for ERS-1 to cover almost the entire globe, up to N 84.6°.

Some of the key characteristics of the ERS-1 SAR are listed in Table 1.

2.4 Current and Future SAR Sensors

For the moment there are two operational polar orbiting satellites carrying SAR instruments, ERS-2 and RADARSAT. The SAR instrument on ERS-2 is similar to ERS-1 SAR while the SAR on RADARSAT has the ability to shape and steer its radar beam, achieving up to five times larger area coverage than the ERS SARs. SAR images from RADARSAT are currently used operationally in the Swedish ice breaking services.

RADARSAT is a commercial, Canadian satellite launched in November, 1995. Using a single frequency, C-Band, the RADARSAT SAR has the unique ability to shape and steer its radar

beam over a 500 km range. Depending on the swath the resolution varies from 8 m to 100 m. The incidence angles has a large range between 20°-50°. The satellite has a repeat cycle of 24 days. However, due to the steerable beam, a location can be viewed more frequently than with ERS-2. RADARSAT SAR has HH polarisation (horizontally transmitted, horizontally received) which is an advantage within the ice applications, since this type of polarisation makes it easier to distinguish between open water and thin new ice. However, Envisat-1, with a more advanced antenna concerning polarisation modes, is waiting to be launched.

Envisat-1, an environmental research satellite of European Space Agency, is scheduled to take over after ERS-1/2 in November 1999. It will carry an Advanced Synthetic Aperture Radar (ASAR) besides a large amount of other instruments. The ASAR, operating at C-band, will have an array antenna equipped with distributed transmit/receive modules offering the ability to provide different combination of polarizations. ASAR will also be able to scan in a similar way to RADARSAT.

3 Backscatter Theory

The amount of energy reflected from a surface covered by the radar signal, depends on the physical characteristics of the surface. The energy reflected is described by the radar cross section, σ, defined as the cross section area of a metallic sphere, with a radius $>>$ radar wavelength, that scatters the same energy as the illuminated target.

$$\frac{\delta\sigma}{\delta A} = \sigma^0 \qquad (5)$$

9

Parameters	Values
Radar frequency	5.3 GHz (C-band)
Radar wavelength	0.056 m
Spatial resolution along track	30 m
Spatial resolution across track	26 m
Swath width	100 km
Localisation accuracy	1 km
Antenna dimensions	10 m long, 1 m wide
Incidence angle	19-26°, 23° from nadir at mid swath
Polarization	vertical-transmit, vertical-receive
Transmitted pulse length	64 ns
Pulse frequency repetition	299 μs
Transmitted peak power	4.8 kW

Table 1: Key characteristics of the ERS-1 SAR.

Figure 8: The mean scattering cross section per unit area.

where σ^0 is the mean scattering cross section per unit area [LDKM95], see Figure 8. σ^0 is used in practice, since averaging over an area is necessary due to speckle. Note that σ^0 is dimensionless and due to the range of values σ^0 is usually expressed in decibels.

$$\sigma^0_{(dB)} = 10 \cdot \log_{10}(\sigma^0) \qquad (6)$$

where σ^0 of 0 dB is equivalent to 1 m^2 cross section of a sphere per 1 m^2 ground area.

3.1 Backscatter in General

The geometry and the electrical features, e.g. the dielectrical constant, are the main surface characteristics that effect the backscattering [Ela88]. The geometry is defined by parameters such as slope and roughness, see Figure 9. The dielectrical constant of a material depends, among other variables, on its water content, temperature and salinity. The imaginary component of the dielectrical constant represents the ability of a medium to absorb the radar wave. The

10

Figure 9: Backscatter as a function of incidence angle and roughness. Backscattering from natural surfaces usually consists of a combination of specular returns from facets near vertical incidence and Bragg scattering from large angles.
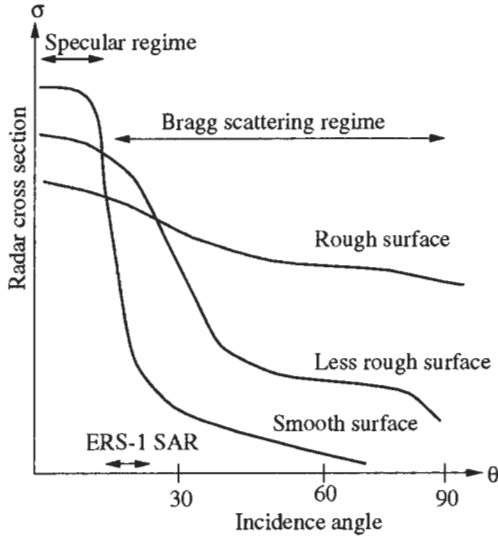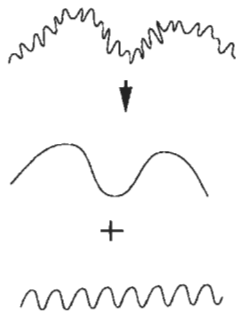

Figure 10: Subdivision of rough surfaces into their Fourier spectral components.

backscattered signal decreases with increasing liquid water content in the propagation medium, due to absorption which decreases the penetration depth [Ela88].

Beside surface characteristics, σ^0 depends on parameters as wavelength, polarisation and incident angle of the radar signal. The longer the wavelength of a signal is, the deeper the signal penetrates into the material. The microwave wavelengths are within the range of 0.1 - 300 cm. A signal of the longest wavelength penetrates about ten times deeper than a signal of the shortest wavelength [Ela88]. ERS-1 SAR signal has a penetration depth of the order of centimetres.

The incidence angle plays a crucial role for the backscattering. The impact of incidence angle in combination with roughness, can be seen in Figure 9. For small incidence angles, less than 20°, specular reflections from facets dominates the returned signal. In the case of incidence angles between 20° and 70° the dominating mechanism of the reflected signal is the Bragg scattering. A rough surface can be subdivided into its Fourier spectral components, see Figure 10. Bragg scattering is a mechanism where the reflected signal from some of these surface components resonates with the incident wave [Ela88]. Incidence angles larger than 70° give a weak backscatter that can be described as a modified Bragg scatter, since large targets have a shadowing effect on the signal. ERS-1 SAR has an incidence angle between 19°-26°. Backscattering from natural surfaces usually consists of a combination of specular returns from facets near vertical incidence and Bragg scattering from large angles.

Due to the variation of the radar incidence angle across the swath, the pixel values are slightly higher at near edge, since SAR looks more nadir there compared to far edge. Also, the difference

in distance between near and far edge gives a more faded signal from the far edge. No calibration method can prevent the influence of change in backscattering, due to the incidence angle.

3.2 Snow and Sea Ice Backscatter

When an electromagnetic wave reaches an interface separating two media, the wave is partly transmitted and partly reflected, depending on the electromagnetic characteristics of the two media. When the radar signal reaches the sea ice, there are three main surfaces that can effect the wave: atmosphere/snow surface, snow/ice interface and ice/water interface [Car95]. Volume scattering due to inhomogeneities within the different layers does also interact with the radar signal.

If the snow cover on the ice is dry the microwave signal penetrates through the snow and interacts with the ice surface underneath. On the other hand, if the snow is wet the penetration depth of the radar signal decreases and the signal is scattered from the snow cover. The snow becomes visible for the radar. At the same time the backscattered signal decreases due to absorption in the wet snow layer. A snow layer is more visible for high frequencies [Ela88]. The snow surface roughness, grain size and possible ice crusts within the snow layer are other parameters that effect the backscatter from the snow cover.

Surface roughness is the main factor effecting the backscattering from ice. Air bubbles in the ice scatter the signal due to inhomogeneities, i.e. change in the dielectrical constant. Salinity and temperature of the sea ice affect σ^0 indirectly, since they effect the volume of brine pockets, leading to inhomogeneities in the ice and also absorption of the signal by brine [Car95]. If salinity and temperature are low, as in the Baltic Sea,

the air bubbles in the ice get a more significant role as a backscatter mechanism. In the Baltic Sea, for the frequency, polarization, amplitude and incidence angle of ERS-1 SAR, the principal backscatter mechanism is the scatter from the snow/ice interface [UJA92]. The backscatter from deformed ice is dominated by specular reflections, while level ice effects the signal by small-scale surface roughness (Bragg scattering) [Car95]. Since the value of a pixel is an average in SAR images, deformed ice affects the pixel value although it only covers a fraction of the pixel.

The ice/water interface is only reached by long microwaves due to the effects of absorption [Car95].

4 Weather and Ice Conditions

The winter 1994 can be defined as normal, since the whole Gulf of Bothnia and the northern part of the Baltic Proper were ice covered in the beginning of March.

The ice season started in late November 1993 during a period of cold weather, with ice formations in the archipelagos in the Gulf of Bothnia. However, this period was overtaken by warm winds from the south, packing the ice along the northernmost part of the Bothnian Bay. In January the ice formation took place in the open sea in Bothnian Bay, with some ridge formations. The cold weather covering Scandinavia, continued even in February and was characterised by a high pressure system with weak northeasterly winds and cloudless conditions over the Baltic Sea. During this period the ice conditions in the Bothnian Bay was stabilized and only minor changes in the ice formation took place in late February and March. The Bothnian Sea was

12

ice covered during this period, but with varying conditions in the western part due to an easterly ice drift. Maximum ice extent was obtained in March 3 to 4 1994. A few days later strong winds from south broke up the ice in the southern Bothnian Sea and created strong ice pressure with ridge formations in the northern part. In the end of April, the ice concentration started to decrease in the Bothnian Bay and in mid May the western part was ice free with open water, whereas some ice was left along the Finnish coast. This ice-break-up occurred about one week earlier than normal [Car94].

5 Data Description

5.1 Meteorological Data

The meteorological conditions in the area covered by the SAR images is best represented by the weather stations Storöhamn, Haparanda and the lighthouse Farstugrunden, see Figure 1. According to [MH94], Storöhamn and Haparanda weather stations show no significant difference between each other in the weather parameters. Since Storöhamn is situated on a peninsula in the middle of the image area it should be the most relevant. Weather station Farstugrunden has a more remote position and is chosen to represent the more maritime weather conditions.

The daily means of air temperature, relative humidity and precipitation have been used. Farstugrunden does not make observations of precipitation. Due to the maritime location of Farstugrunden weather station, it shows a slightly higher temperature than Storöhamn, see Figure 11.

The air temperature and relative humidity were used to calculate the water vapor content of air, so called mixing ratio [WH77]. The mixing ratio shows a high correlation with air temperature, see Figure 11.

5.2 Image Data

A time series of 17 SAR Low Resolution Images (LRI) were used in this study. LRI are down loaded and processed at Tromsø Satellite Station (TSS). They are generated from the Full Resolution Image (FRI), which is similar to ESAs ERS-1 UI16 Fast Delivery (FD) Product with pixel size 20 × 15.8 m (range direction × azimuth direction). The SAR LRI product size is computed by reducing the SAR FRI product size by a factor 25 (5 × 5 pixels) giving a resolution of 100 × 80 m (range direction × azimuth direction).

The images were recorded during the second ice orbit phase of ERS-1. This orbit was configured such that a given area was covered every third day. The images were registered during descending path in the morning at 10 UTC and short after received via Internet by SMHI to be used in The Baltic Experiment for ERS-1 (BEERS) in winter 1994. The images were then stored on Exabyte cassettes as 16-bits images.

17 images cover the period 940113-940407. The dates of the images are listed in Table 2. Since some images were geometrically deformed, probably due to failure in the data processing or deviations in the satellite orbit, the area is not covered exactly every third day.

An original ERS SAR image covers an area of 100 km × 100 km. In this study only a part of the image area is used. This is partly because of the calibration and partly because the images should only cover fast ice, since the main idea of this study is to analyse ice that is not affected by any dynamical forces. The location of the subimage covering 59 × 26 km, can be seen in Figure 1 and 2. The images consist of 590 × 330
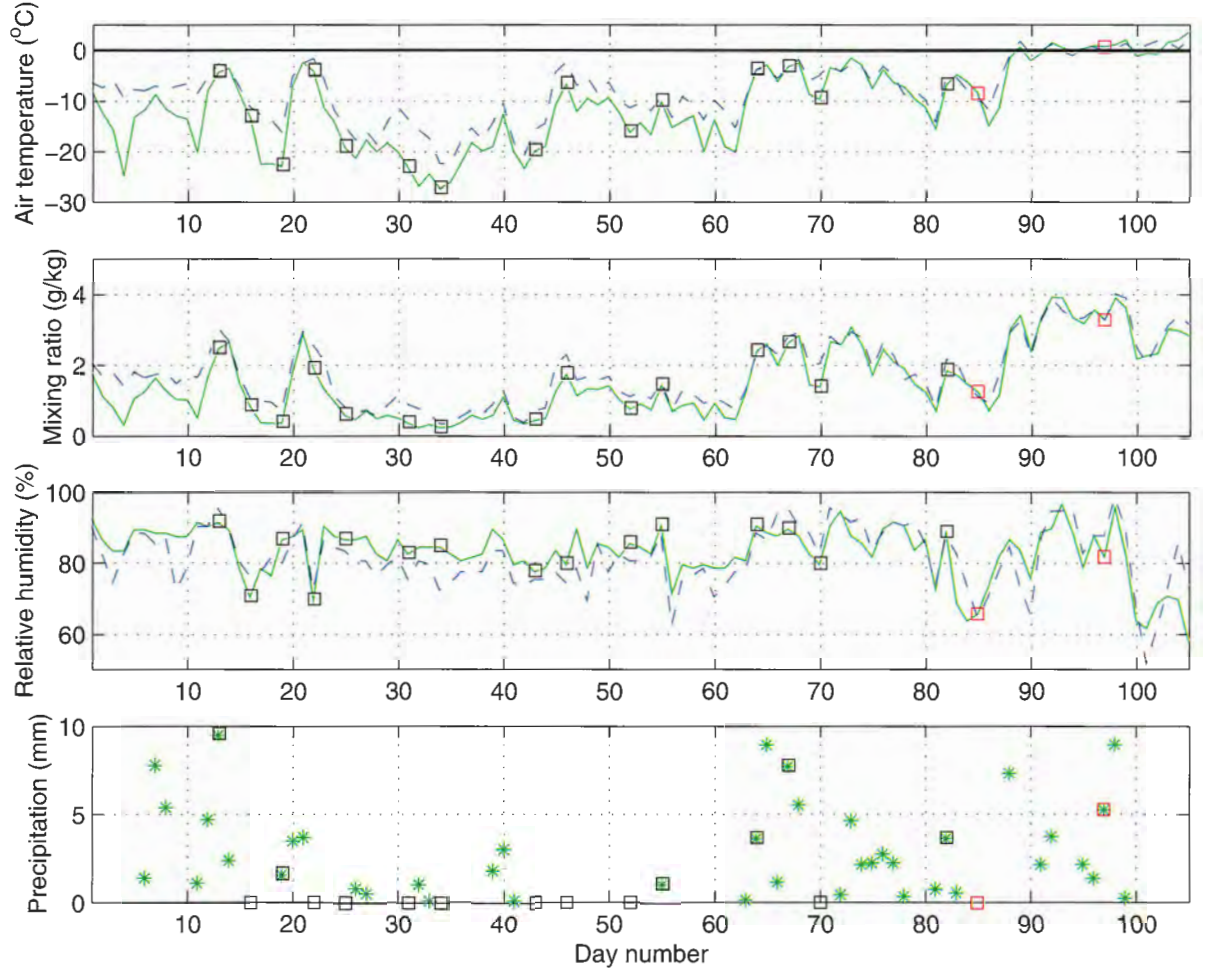
13

Figure 11: Weather parameters during the period 940101-940415. Green and blue lines represent Storöhamn and Farstugrunden weather stations respectively. Precipitation is only measured at Storöhamn weather station. The dates of the SAR images are marked with squares. The two red squares represent the last images in the time series, discussed separately in Section 8.4.

January	February	March	April
13	3	5	7
16	12	8*	
19*	15	11	
22*	21*	23	
25	24	26*	
31			

Table 2: The dates of the images. A star marks the images used for calculation of the calibration constant, see Section 6.3.

pixels. The location of the subareas differs from scene to scene but they are all within the limit of the range correction, see Section 6.2. The images are geographically adjusted manually.

Six ERS-1 UI16 Fast Delivery (FD) images were used to calculate the calibration constant of the LRI. FD images are received from Kiruna receiving stations. Table 3 shows some of the characteristics of the two types of images used in this study.

6 Calibration of LRI Images

There are different kinds of calibrations of SAR images e.g. geometric, phase (see Figure 7) and radiometric calibration [Fre92]. Geometric calibration means to adjust the image coordinate system to a reference surface. One kind of phase calibration is to relate a phase difference between two SAR images to a topographical height. It is called interferometric calibration and is used for example to see how fast glaciers grow. For explanation of phase within a SAR pixel element, see Figure 7.

6.1 Radiometric Calibration

In this thesis radiometric calibration has been performed on the LRI images. Radiometric calibration has been chosen because it relates the pixel value to a radar backscatter value, σ^0, which is a measure of the surface characteristics independent of the SAR system parameters. Radiometric calibration is therefore used with multichannel SARs, because it makes it possible to compare data from different SAR sensors.

The radiometric calibration of LRI is based on the calibration of two other types of images, PRI (Precision Images) and FD images. According to [LBM+98], the following relation is valid to calculate σ^0 in a PRI.

$$\sigma^0 = (< DN^2 > - (DN_n)^2) \frac{1}{K} \frac{\sin \theta}{\sin \theta_{ref}} C \frac{PRP}{RRP} Pl \quad (7)$$

where

- DN (Digital Number) is the pixel value. $<>$ stands for spatial averaging over the area of interest. The value of one pixel has little statistical significance due to the speckle and must therefore be averaged.

- K is the calibration constant which is specific to the type of data product and to the

Product	LRI	FD (UI16)
Pixel size (range × azimuth)	100 m ×80m	20.0 m × 15.9 m
Resolution (range × azimuth)	100 m × 80 m	25 m × 22 m
Bits	16	16
Looks	3	3
Receiving station	Tromsø	Kiruna

Table 3: Characteristics of the LRI and FD image products.

processing centre. The calibration constant is discussed in Section 6.3.

- $\frac{\sin \theta}{\sin \theta_{ref}}$ is the change in scattering area on ground with increasing incidence angle, θ. This factor will be discussed further in Section 6.2.

- C is the factor that accounts for updating the gain. Due to the antenna pattern, corrections for the antenna gain have to be performed on the images. This is implemented in the processing of the PRI. Since the gain correction has improved during the life time of ERS-1, C is needed to compensate for this in the calibration.

- PRP stands for Product Replica Power and RRP stands for Reference Replica Power. The replica pulse works like a control pulse for the SAR system and is applied on the images through the gain normalisation. The replica pulse correction factor is a correction for the unwanted variations of this control pulse.

- Pl stands for Power loss and is a correction due to the problem of saturation of the Analogue to Digital Converter (ADC). It is mainly a problem for large distributed targets having high backscatter coefficients

[LBM$^+$98], as for example, open water areas under windy conditions, large cities and the ice sheet on Greenland.

- DN_n is the root mean square (rms) noise pixel value. The noise includes contributions from for instance the Earth microwave background radiation and thermal noise in the antenna.

According to [Ula94]

$$DN_n^2 = K \cdot (-25.5dB \pm 0.5dB) \qquad (8)$$

where $-25.5dB \pm 0.5dB$ is a reference value of the noise-equivalent backscattering coefficient found in the PRI header.

According to [Ula94] the following relation is valid to calculate σ^0 for FD images:

$$\sigma^0 =$$
$$(< DN^2 > - DN_n^2)\frac{1}{K} \cdot$$
$$(\frac{R}{R_{ref}})^3 \frac{\sin \theta}{\sin \theta_{ref}} \frac{G^2(\nu_{ref})}{G^2(\nu)} \qquad (9)$$

where $(\frac{R}{R_{ref}})^3$, representing the range spreading loss, is added compared to Equation 7. The correction for the range spreading loss is applied already at the processing step on PRI images but not on FD images, why this must be done in the calibration. The same is true for the antenna

16

gain factor, $\frac{G^2(\nu_{ref})}{G^2(\nu)}$ which has not been applied on the FD at processing. Since no antenna gain normalisation has been performed on the FD images, the Replica Power correction from Equation 7 is not needed in Equation 9 [Ula94]. The phenomenon of power loss was not known when Equation 9 was written, even though it is a problem for FD in the same way as for PRI.

LRI are averaged FRI which are similar to FD images. It means that LRI have the same characteristics as FD and Equation 9 is assumed to be valid for LRI images including the powerloss factor from Equation 7. However, the saturation is mainly a problem over large distributed targets with high backscatter coefficients like open water areas under windy conditions. Since this study focus on sea ice, no correction for saturation is applied in the calibration. Hence, the following equation is valid to calculate σ^0 values in LRI:

$$\sigma^0 = \frac{f}{K}(<DN^2> - DN_n^2)$$ (10)

where f is the range correction, see Equation 11 below. Calibration constant K is specific to the type of data product and a calibration constant, K_{LRI}, for LRI will be determined in Section 6.3.

6.2 Range Correction, f

In this section, the parameters calibrating the backscatter signal in range direction will be discussed. Since the SAR antenna looks obliquely in different angles, the backscattered signal has to be compensated for the geometry over the swath. Figure 12 shows the geometry of ERS-1 SAR.

The factors correcting the backscatter in range direction can be concluded in the range correction factor, f, which is given by the following
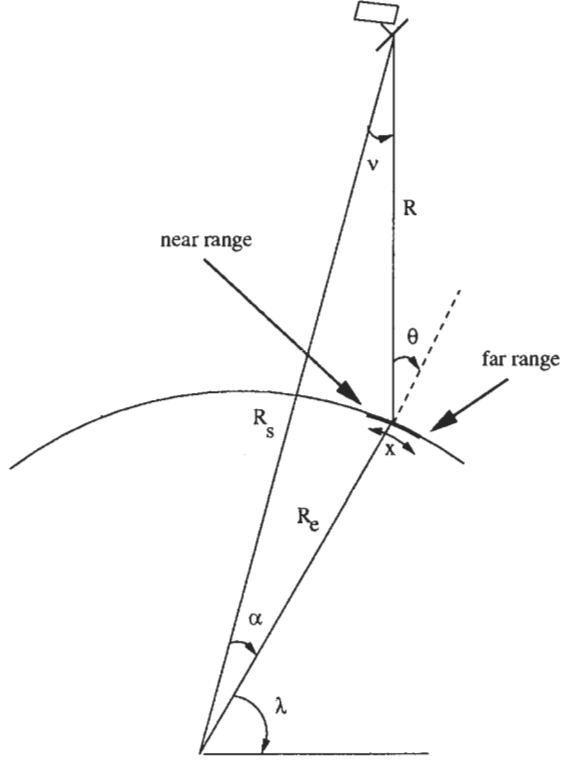

Figure 12: Geometry of ERS-1 SAR. R is the distance between satellite and target. θ is the incidence angle. ν is the antenna elevation angle, also called look angle. $\theta > \nu$ due to the curvature of the earth surface.

equation [Ula94]:

$$f = \left(\frac{R}{R_{ref}}\right)^3 \frac{\sin\theta}{\sin\theta_{r}ef} \frac{G^2(\nu_{ref})}{G^2(\nu)} \qquad (11)$$

where the first term represents the range spreading loss and the second term accounts for the change in scattering area on ground, with increasing incidence angle. The last term is compensation for the antenna pattern which describes the form of the illuminated beam. Since the antenna does not spread the signal homogeneously in all direction, a correction has to be made. The antenna pattern used is received from the look-up table *Improved ERS-1 SAR Elevation Antenna Pattern* [LBM+98]. The reference values in Equation 11 are: $R_{ref} = 847$ km, $\theta_{ref} = 23°$ and $\nu_{ref} = 20.35°$. ν_{ref} is the antenna boresight angle. R, θ and ν, see Figure 12, are calculated across the swath in Appendix A. Since these parameters can not be exactly determined from the information given in the image file header, the image swath is assumed to be an curve of exactly 100 km. According to [Ula94] this assumption results in a calibration error of ±0.25 dB.

Due to the stable orbit of ERS-1, the look angle of the SAR antenna is very stable, ± 0.03° [Ula94], and it is often sufficient to use a single range correction for all images in the same region and for a single kind of orbit phase. The calibration is restricted to the 10 - 90 km swath, due to the strong fall of the antenna gain pattern at the edges, which increases the uncertainties [Ula94]. As described in Section 5.2, only part of the original image area is used in this study. The area used is within the 10 - 90 km limit in all cases. The values of the range correction across the whole swap can be seen in Figure 13.

6.3 Calibration Constant, K_{LRI}

The calibration constant fits the brightness level of the image product, to the radar backscatter level, σ^0. Since no official calibration constant exists for LRI, K_{LRI} is estimated from FD images for which a calibration constant is defined. Since σ^0 has the same value independent of image product, the following expression from Equations 9 and 10, neglecting the powerloss factor, is valid:

$$\frac{f}{K_{LRI}}(< DN^2_{LRI} > -DN^2_{nLRI}) =$$
$$\frac{f}{K_{FD}}(< DN^2_{FD} > -DN^2_{nFD}) \qquad (12)$$

where the suffix FD and LRI denotes the different images. DN^2_{nLRI} and DN^2_{nLRI} are given by Equation 8. Simplification gives

$$< DN^2_{LRI} >= \frac{K_{LRI}}{K_{FD}} \cdot < DN^2_{FD} > \qquad (13)$$

which shows the relation between the pixel values in LRI and FD images, respectively.

Six LRI and FD images from the same satellite passes, covering the same area, were used to calculate the K_{LRI}. Images from the dates 940119, 940122, 940221, 940308, 940320 and 940326 were used. Each image was divided into 10 parts in azimuth direction and into 16 parts in range direction within the 10-90 km limit. In Figure 14 the relation in Equation 13 is plotted for each area mean in the 160 subareas. Due to change of SAR data processor at Tromsø Satellite Station in March 1994, the pixel values of the LRI images decreased in brightness level. The decrease can clearly be seen in Figure 14 where two lines shows the relation between the pixel values in the LRI and FD images. The circles represent the period before the change of processor,
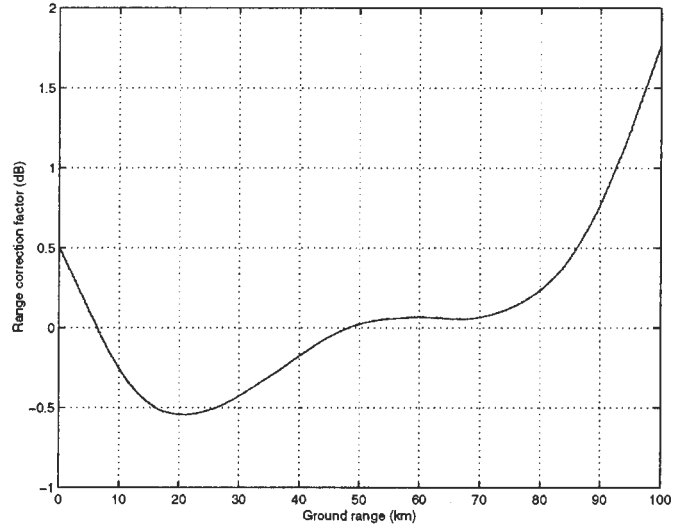
Figure 13: Range correction across the swath. Due to strong fall of the antenna gain pattern at the edges, the range correction is only valid within the 10-90 km swath.

Figure 14: The relation between the pixel values in LRI and FD images. Circles represent the scenes from 940119, 940122, 940221 and 940308. Stars represent the scenes from 940320 and 940326.

19

Figure 15: Linear relation between the pixel values in LRI and FD images represented by scenes from 940119, 940122, 940221 and 940308. The blue line represents the linear trend in the data and the red lines represent the standard deviation from the blue line.
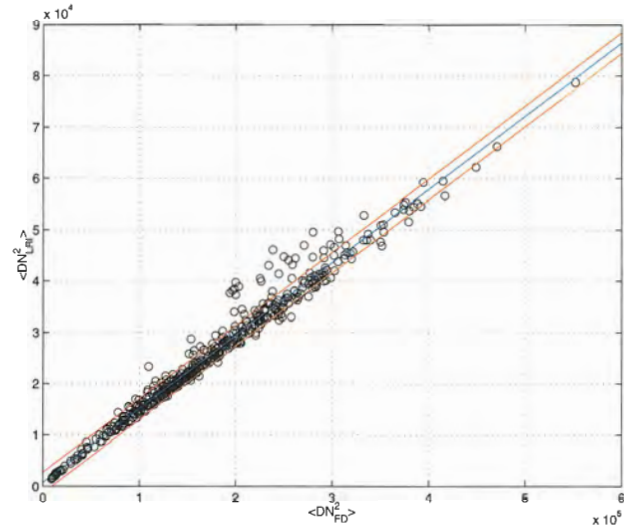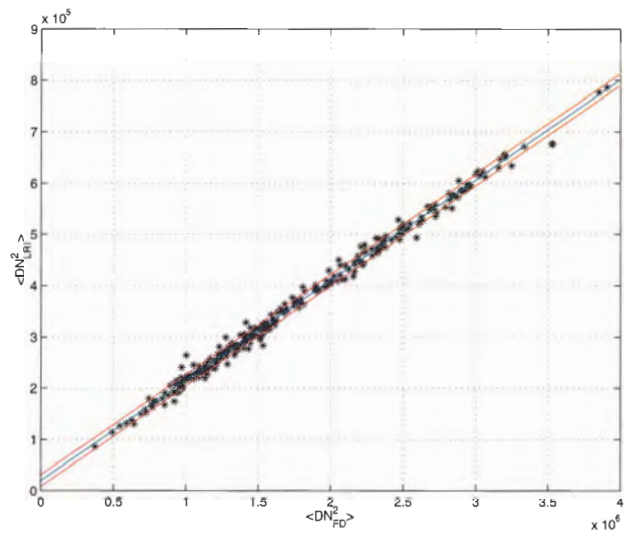

Figure 16: Linear relation between the pixel values in LRI and FD images represented by scenes from 940320 and 940326. The blue line represents the linear trend in the data and the red lines represent the standard deviation from the blue line. Note the difference in scale relative Figure 15.

Date	Calibration constant (dB)	Accuracy (dB)
940113-940311	54.6	0.5
940320-940407	65.9	0.7

Table 4: Calibration constants of the LRI images.

940113-940311 and the stars represent the period after, 940320-940407. The relations are linear where the slopes of the lines are described by the factor $\frac{K_{LRI}}{K_{FD}}$ in Equation 13. The lines result in two different calibration constants during the period of the time series. The FD image calibration constant, K_{FD}=73.0 dB [MPAH97], [Ula94], was used to calculate K_{LRI}.

K_{LRI} is determined to $(54.6 \pm 0.5)dB$ during the first period of time and to $(65.9 \pm 0.7)dB$ during the second period. Figure 15 and 16 show the relations between $< DN_{FD}^2 >$ and $< DN_{LRI}^2 >$. The red lines show the standard deviation from the linear trend. In table 4 the two determined calibration constants are summarized.

The range correction, the calibration constant and rms noise pixel value are the components included in the calibration of LRI. The dominating errors are the range resolution with an accuracy of 0.25 dB and the calibration constant with an accuracy of 0.7 dB in the worst case. By taking unknown errors into account, the calibration error is estimated to ± 1 dB.

7 Empirical Orthogonal Functions (EOF) Theory

Empirical Orthogonal Function analysis was carried out on the images in order to study the time variability of the whole image area. Analysis and results are described in Section 8.5. This section gives an introduction to the EOF theory.

Empirical Orthogonal Functions (EOF) [Pre88] are found within the large statistical field of Principal Component Analysis (PCA). PCA is a statistical technique to describe a data set with a decreased number of variables, to which the main part of the variance is concentrated. That simplifies the analyse of, for instance, a time series of satellite images which contains thousands of variables, each one represented by one pixel. There are different definitions of Principal Components in relation to Empirical Orthogonal Functions in the literature. In this thesis the Empirical Orthogonal Function is a Principal Component normalised to the length 1, as in [Jol90]. It should be noticed that the statistical EOFs do not necessarily have any physical meaning and should only be used as indicators of physical relations. The equations and symbols in this section are mainly from [ET98].

7.1 Spatial and Temporal Functions

The aim is to find a set of orthogonal spatial functions, $\phi(\mathbf{x})$, of certain conditions, see below, in order to express the data set as in Equation 14.

$$\psi(\mathbf{x}_m, t) = \psi_m(t) = \sum_{i=1}^{M} a_i(t)\phi(\mathbf{x}_m) \qquad (14)$$

The data $\psi(\mathbf{x}, t)$, in Equation 14 is collected at M locations but the equation describes the data series at the m:th location $\mathbf{x}_m$. $a_i(t)$ is a
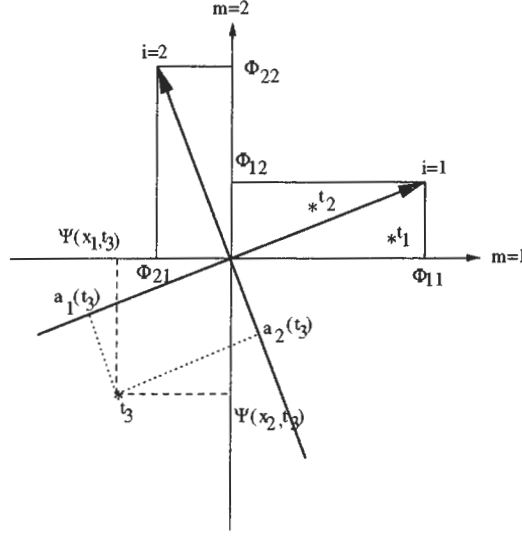
Figure 17: $\psi(\mathbf{x}, t)$ measured at two locations, $\mathbf{x}_1$ and $\mathbf{x}_2$, each location representing one dimension. The variable is measured at three occasions, t_1, t_2 and t_3. i represents the orthogonal spatial functions.

temporal function describing the amplitude of the i:th orthogonal spatial function at time t, see Figure 17.

Figure 17 shows an example of $\psi(\mathbf{x}, t)$ measured at two locations, $\mathbf{x}_1$ and $\mathbf{x}_2$, each location representing one dimension. The variable is measured at three occasions, t_1, t_2 and t_3. The figure illustrates how the method simply describes a rotation of the coordinate system, where the "new" spatial functions are described by coefficients $\phi_i(\mathbf{x})$ of the old base $\mathbf{x}$, see Equation 15. $a_i(t)$ is called the modal coefficients and is the time series projected on respective spatial function.

$$\psi(\mathbf{x}, t) =$$
$$\begin{bmatrix} a_1(t_1)(\phi_{11}, \phi_{12})\mathbf{x} + a_2(t_1)(\phi_{21}, \phi_{22})\mathbf{x} \\ a_1(t_2)(\phi_{11}, \phi_{12})\mathbf{x} + a_2(t_2)(\phi_{21}, \phi_{22})\mathbf{x} \\ a_1(t_3)(\phi_{11}, \phi_{12})\mathbf{x} + a_2(t_3)(\phi_{21}, \phi_{22})\mathbf{x} \end{bmatrix} (15)$$

As mentioned before, certain conditions are re-quired for the spatial functions. Since the procedure describes a rotation of the M-dimensional coordinate system, the spatial functions are orthogonal so that they form a set of basis functions.

$$\sum_{m=1}^{M} (\phi_{im}\phi_{jm}) = \delta_{ij} \qquad (16)$$

The Kronecker delta is defined by

$$\delta_{ij} = \begin{cases} 1 & , \quad j = i \\ 0 & , \quad j \neq i \end{cases} \qquad (17)$$

To make the PC:s unique, the time amplitudes $a_i(t)$ are uncorrelated.

$$\overline{a_i(t)a_j(t)} = \lambda_i \delta_{ij} \qquad (18)$$

gives that λ_i is equal to the variance of each orthogonal mode according to

$$\lambda_i = \overline{a_i(t)a_i(t)} = \frac{1}{N} \sum_{n=1}^{N} (a_i(t_n)^2) \qquad (19)$$

22

where N is the number of samples, $t_1 \cdots t_N$.

7.2 The Eigenvalue Equation

By forming the covariance matrix $\overline{\psi_m(t)\psi_k(t)}$ and using Equation 16 and 18 to simplify the expression, the following eigenvalue problem can be found [ET98].

$$\sum_{k=1}^{M} \overline{\psi_m(t)\psi_k(t)}\phi_{ik} = \lambda_i\phi_{im} \qquad (20)$$

where the PCs, ϕ_{im} are the eigenvectors and λ_i the corresponding eigenvalues. This means that the eigenvectors associated with the nonzero eigenvalues of corresponding covariance or correlation matrix, represent a set of orthogonal base vectors which fulfill the requirements in Equation 16 and 18. The eigenvector with the highest eigenvalue represents the first Principal Component and has the direction of the largest variance in the M-dimensional space, while the second eigenvector is perpendicular to the first and keeps the second largest variance.

Another proof of this statement, starting in the other end, can be read in [RJ96]. It describes how the direction of the greatest variance is found from the eigenvectors of the correlation matrix, based on the equation of the hyperellipsoid the data points are forming. The hyperellipsoid is centered, since the mean value of the time series at each location are removed from the data set, $\psi(\mathbf{x}, t)$.

8 Analysis and Results

In this section, the analysis of the 17 calibrated images in the time series will be presented. To start with, 21 separated areas of different surfac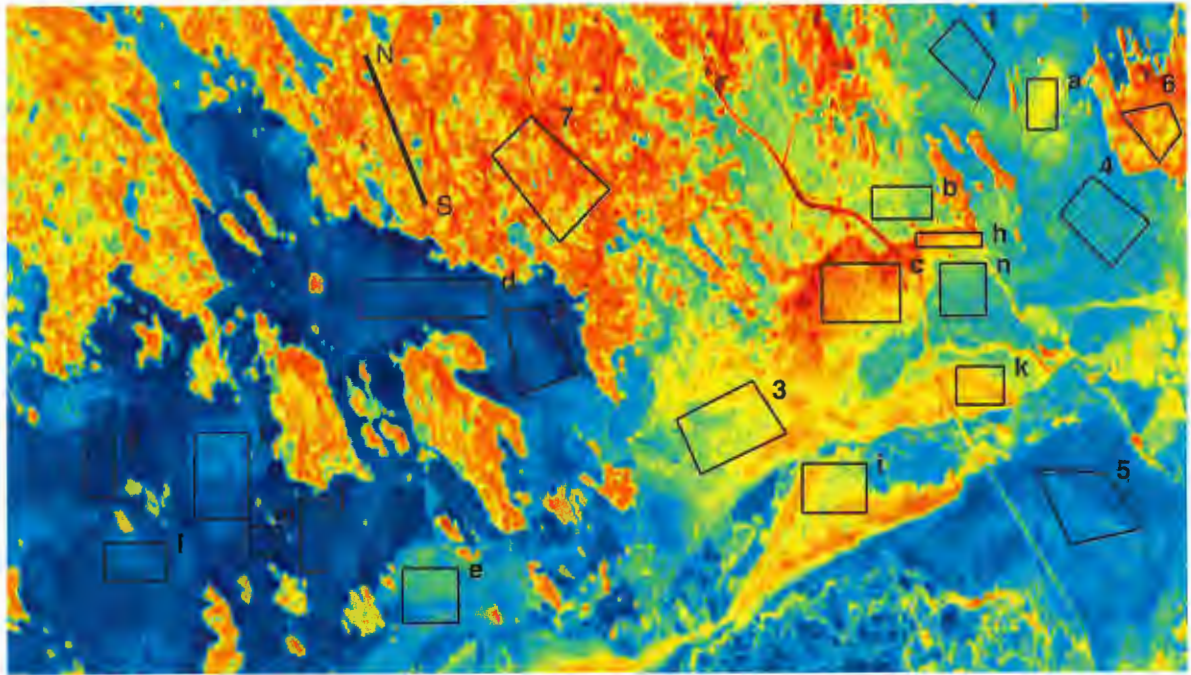e characteristics are analysed. In Section 8.1 the time series of the mean backscatter coefficients of the 21 subareas are shown. The temporal and spatial variations of the areas are discussed in Section 8.2. In Section 8.3 a classification based on the temporal standard deviation values, texture and backscattering coefficient of the 21 areas is made and compared to contemporary values.

Section 8.4 presents a case study of the two last images in the time series which represent cold and mild weather respectively. In Section 8.5 the 21 subareas are extended to the whole image area, by using EOF analysis in order to get an overview of the weather dependence of the backscatter coefficient.

This section begins with an explanation of the temporal mean image of the 17 calibrated images. The geography of the image area and the ice formations that can be seen in the mean image are described. As mentioned in Section 5.2, the area is chosen within the fast ice in order to avoid movements in the ice cover. Still, there are large variations of ice formations within the area, as can be seen in Figure 18. The sea area of the images is characterised by low salinity due to high discharge of fresh water from several large rivers. The area is shallow within the archipelago.

The figure shows the temporal mean image with 21 marked areas representing different types of ice. Those areas will be further discussed in later sections. The high backscatter areas in the upper part of the image are land, while the very high values found at area c and further down in the image are due to very rough ice. The rough ice is jammed brash barriers, consisting of small ice blocks which work as facets giving a very strong backscattering due to many small local incidence angles. Those ice formations were created by southerly winds resulting

23

26 km

0 km   59 km

−20   −18   −16   −14   −12   −10   −8   −6   −4 (dB)
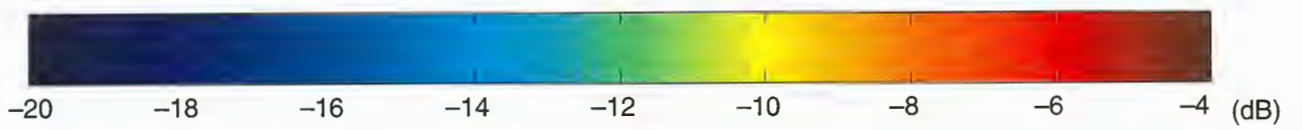
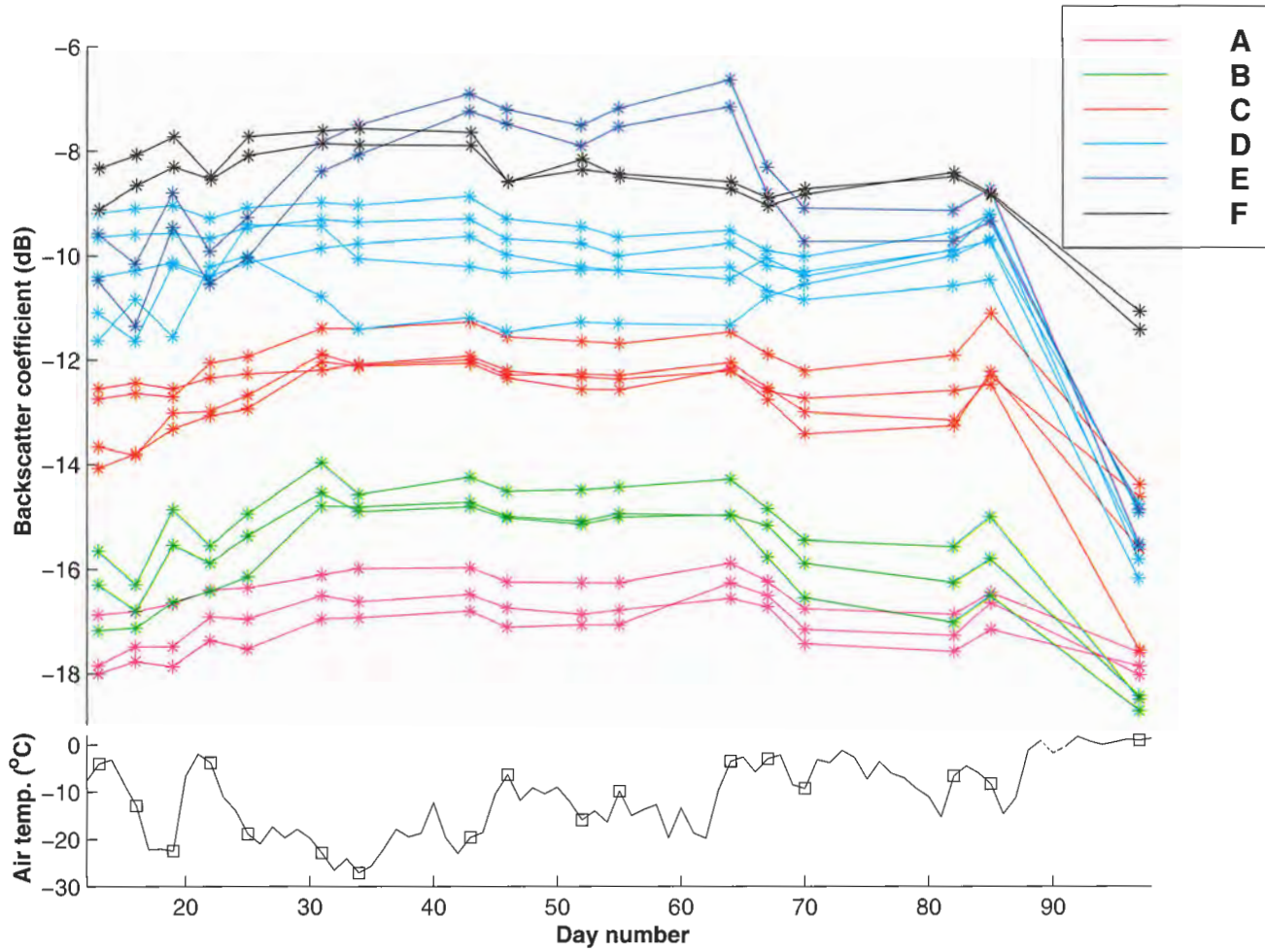Figure 18: The temporal mean image of the 17 calibrated images. 21 areas showing different surface classes are marked.

24

Figure 19: The mean backscatter coefficient of the areas marked in Figure 18 and the air temperature vs time. The capital letters, $(\mathbf{A} - \mathbf{F})$ refer to the surface classes in Table 5. The dates of the SAR images are marked.

in strong ice-pressure during early winter. The bright line running from the lower right corner up between b and c is a ship track. The cracked ice along the track gives a strong backscattering. The ship track goes to Karlsborg, a harbor south of Kalix. Cities and villages can clearly be seen in the mean image due to the strong radar backscattering from man-made features. The island with area number 6, on the right border of the images, is Seskarö. In the surroundings of area number 5, belts of ridges can be seen. According to the σ^0 value in the mean image, the level ice in the left part of the images are smoother than in the right part.

From the ice chart, it can be seen that the level ice thickness in the area was about 300-450 mm in the beginning of the period and then increased to 500-700 mm in late March. The ice is snow covered during the period of the images but it is difficult to tell the thickness of the snow cover, since the snow distribution varies due to wind and surface roughness. Also, no measurements were made in the area during the period. On land the snow thickness is between 800-900 mm. Snow depth measurements made on the ice at Ratan, varied between 100-300 mm during the period. Ratan is located north of Umeå, about 150 km south of the image site.

8.1 Correlations between Mean Backscatter Coefficients and Weather Parameters.

This section describes the time series of the mean backscatter coefficients of the areas, marked in Figure 18. Also the correlation between the mean backscatter coefficients and weather parameters are shown.

The time variations of the mean backscatter coefficients of the areas and the air temperature are shown in Figure 19. The colours represent the surface classes, $\mathbf{A} - \mathbf{F}$, defined in Section 8.3.

The uncalibrated gray level variations of site $\mathbf{1} - \mathbf{7}$ have been investigated in [MH94]. The gray levels showed no significant correlation with air temperature, except for the land areas $\mathbf{6}$ and $\mathbf{7}$. The same result can be seen in Table 11, Appendix 8.1, where the correlations between the mean backscatter coefficients and weather parameters are shown. The land areas show significant correlation [2] both with air temperature and air water content. Four of the marked ice areas show significant correlation with air water content but no ice area correlates with temperature or relative humidity.

This section has shown the mean backscatter coefficients of 21 areas and discussed the correlations between the mean backscatter coefficient and weather parameters which can be seen in Appendix 8.1. Land and four ice areas show significant correlation with weather parameters.

8.2 A Study of Temporal and Spatial Variability

In this section the temporal standard deviation image, normalised by the temporal mean image, is analysed. Note that temporal standard deviation is not the texture being related to a certain surface. Instead the temporal standard deviation image normalised by the mean, represents variation in time. The image describes how the mean level varies between the dates in each pixel.

The temporal standard deviation image is shown in Figure 20. Low values in the image represent low variation in time while high values

---

[2] According to [HH95], the linear correlation coefficient of 17 variables (i.e images) must be $> |0.60|$ in order to give 99% probability that two variables are linearly associated to each other.

26

26 km

0 km   59 km

0   0.1   0.2   0.3   0.4   0.5   0.6

Figure 20: The temporal standard deviation image of the 17 calibrated images, normalised by the temporal mean image.

represent high variations through the time series. Most of the shore lines and boundaries in Figure 20 have high values, since the 17 images are not perfectly geographically orientated to each other. The time variance have little connection to ice type in the temporal standard deviation image. The same values can be found in level ice as in more rough ice.

The areas marked $a - n$ in Figure 20, have been chosen to characterise the different levels of the temporal variation, while areas $1 - 7$ were chosen to characterise different ice types. The mean of those areas in Figure 18 and 20 are plotted in Figure 21. Six surface classes can be distinguished in the plot. As mentioned above, the time dependent variance shows no or very small difference between the classes, except for very rough ice which differs substantially. Instead the ice classes can be determined by their spatial mean σ^0 value.

The texture represents the spatial variation of an area and is calculated from its standard deviation divided by the mean. One method of classification is based on the texture and the backscatter coefficient of the subareas. This can be seen in Figure 22, which shows the texture versus σ^0 of the subareas. The values from the last image in the series, from 940407, is excluded due to differing weather conditions at that date, see further discussions in Section 8.4. Areas 2 and 5 are excluded as well since their areas are not homogeneous and probably contain more than one ice class.

Figure 22 shows that only the backscatter coefficient gives the difference between ice classes, except for very rough ice which differ from the other ice types in texture. Very rough ice can not be distinguished from land, neither in texture nor in backscatter. However, note that the temporal variability in Figure 21 is much higher for areas c and h than for the land areas, 6 and 7. By applying the difference in temporal variability between the two classes in combination with the texture and σ^0 values, a land mask can be created. The following conditions, according to Figure 21 and 22, creates the land mask:

$$\text{land} = \text{true} \quad \text{if} \begin{cases} \sigma^0 > -10\,\text{dB} \\ \text{texture} > 0.32 \\ \text{temporal variability} < 0.35 \end{cases}$$

$$(21)$$

The ice types with the lowest backscatter coefficient in Figure 22, can be separated only if a combination of texture and backscatter is used, since they are within each other's error bars.

Smooth ice differs from rough ice only in σ^0, while very rough ice differs from all other ice classes in all three categories; temporal variability, texture and backscatter coefficient. Land and very rough ice only differ in temporal variability.

8.3 A Seasonal Ice Classification Scheme

From spatial variations in the temporal variability, texture and backscatter coefficient, six classes have been defined in the time series of LRI. In this section the classification scheme is presented and compared to σ^0 values from calibrated FD images from the same period.

The area of the images is complex with many ice types within a small region. In Table 5 a classification of the area is shown. Six classes from Figure 22 have been defined. Three of those classes consist of level ice of different degrees of roughness. One class is land and two represent rough ice. (An English - Swedish glossary of some ice classes can be find in Appendix B.)

In Table 6 σ^0 values of contemporary FD images are shown [DUL94]. These images were reg-
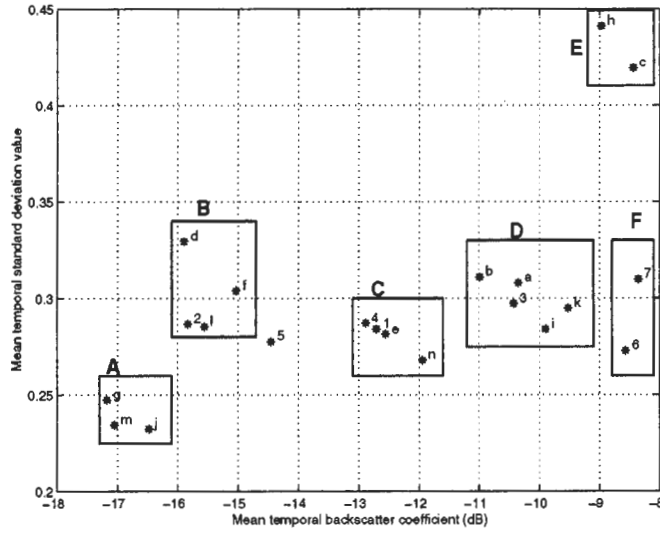
28

Figure 21: The mean values of the marked areas in the temporal mean image versus the mean values of the same areas in the normalised temporal standard deviation image. The capital letters, (**A** − **F**) refer to the surface classes in Table 5.
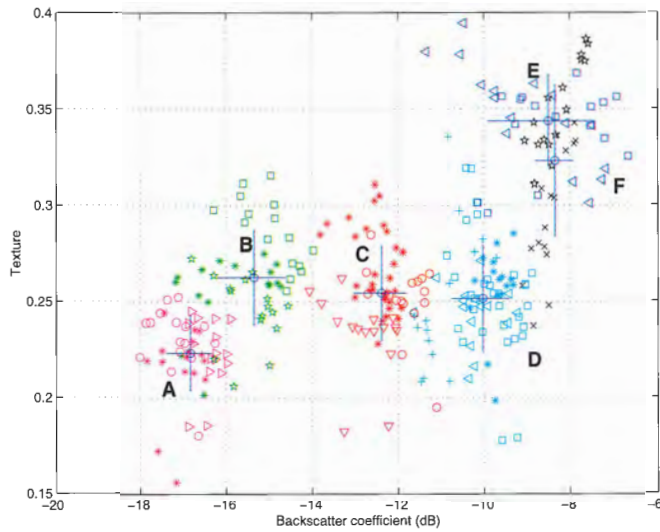

Figure 22: The mean σ^0 values versus the texture values of the marked areas in each image of the time series. A blue ring represents the mean of a class and bars represent the standard deviation from mean. The capital letters, (**A** − **F**) refer to the surface classes in Table 5. The last image in the series, 940407, is excluded. The areas 2 and 5 are also excluded.

Class	Type	Mean σ^0 (dB)	Mean texture
A	Smooth level ice	-16.8	0.22
B	Level ice	-15.3	0.26
C	Rough level ice	-12.4	0.25
D	Deformed ice	-10.0	0.25
E	Jammed brash barrier	-8.5	0.34
F	Land	-8.3	0.32

Table 5: Backscatter coefficients and texture value of six classes from Figure 22. **A-F** refer to the surface classes in the figure.

Ice class	Min σ^0 (dB)	Max σ^0 (dB)
Smooth level ice	-22.0	-17.0
Rough level ice	-17.5	-15.5
Slightly deformed ice	-14.5	-12.0
Ridged ice	-13.0	-9.5
Hummocked ice	-9.5	-8.0
Jammed brash barrier	-11.0	-6.0

Table 6: Backscatter coefficients of different ice classes received from calibrated FD images, March 1994 [DUL94].

istered during cold conditions in the western part of the Bothnian Bay during the dates 940301 and 940304. The texture is not included in Table 6, since a texture value of an FD image is not direct comparable to a texture value of an LRI. The texture of an area decreases with resolution according to [Dam93].

The ice class in the LRI have on average higher σ^0 values than the corresponding class in the FD images in Table 6. As an example, compare the Smooth level ice in the two tables. However, the Jammed brash barrier shows similar values between the two types of images.

The values in Table 6 were not calculated from the same FD calibration constant that was used in Section 6.3. This can be one reason of the differences in σ^0. In addition to that, LRI were calibrated with the improved antenna pattern correction. Since the classification is relative to the types of ice within a single scene, the smooth ice in the fast ice may not necessarily correspond to the smoothest level ice in the drift ice, classified in the FD images. Subjectivity of how the classes are defined could be another reason for the differences in backscatter coefficients between the ice classes.

In this section six classes in the LRI have been defined from spatial variations in the temporal variability, texture and backscatter coefficient. One land class and five ice classes, including two classes of deformed ice and three level ice classes. In comparison to a classification of contemporary FD images, the LRI backscatter coefficients are on average higher.

8.4 Time Variability - a Case Study

In this section, the last two images in the time series are compared as an example of the influence of weather variability on SAR images.

Figure 23 and 24 show the two last images in the time series. The last image , 940407, shows a drastic decrease in backscatter due to mild weather. The ice situation has not changed between the two dates and according to the ice charts in Figure 25 and 26, the image area is covered by fast ice (a diagonal pattern in the ice charts) even at the later date. In [DUL94] it is shown that the number of discriminated ice classes decreases when air temperature rises. That result can also be seen in Figure 23 and 24.

The air temperature was below 0^0C during the whole period until the last days in March, see Figure 11. The red squares in the figure represent the dates of the two images. Also the air wetness increases at the end of the period. Precipitation occurred on the day of the last image, which may have affected the backscatter signal, especially if the temperature is above 0^0C.

Figure 27 shows the contrast between the two images, which gives an overview of the changes between the dates. Negative values (blue colour) in the Figure represent decrease in backscatter values from 940326 to 940407 and positive values (yellow/red colour) represent increased values.

The backscatter coefficient has mainly decreased in areas with rough ice, while level ice is unchanged or shows a weak increase in some areas. Under cold conditions the snow on the ice is dry and transparent for the radar signal. When the snow is wet, the radar signal can not penetrate through the snow layer due to high energy loss and do not reach the ice underneath. It means that in the first image, 940326, where the temperature is below 0^0C and the snow is dry, the signal penetrates through the snow and scatters from the ice surface, while in the last image the backscattering comes from the snow cover. It explains the decrease of backscatter in the rough areas, since wet snow makes rough areas look smoother to the radar. In Figure 11 it can bee seen that precipitation occurred the days before and on the day of the last image. The small variance of backscatter from smooth ice could be due to the fact that the signal level is too small to decrease. There is less snow on plane surfaces due to wind which could be an other reason for the small changes in backscatter on smooth ice. The increase of backscatter in some areas with level ice could occur since the grain size increases in wet snow. It means that the wet snow scatters the signal more than smooth level ice under dry snow during cold conditions [DUL94].

Other contrasts that can be seen in Figure 27 is the red coloured areas which are due to small geometrically displacements between the images. The yellow lines in the lower right part of the images are tracks made of ice breakers between 940326 and 940407 and the red coloured area below, is probably due to movements of the ice near the ice edge.

All areas have more or less decreased in backscatter during the period. Areas with high σ^0 values have decreased more than areas with lower values. Figure 28 shows how the different test sites changed in backscatter and texture between the two dates. Areas within class 5, "Jammed brashed barrier", have decreased most, from -9 dB to about -15 dB. The rate of change in backscattering seems to depend on class, while rate of change in texture varies within the classes. About half of the test areas have increased in texture value and the other half have decreased.
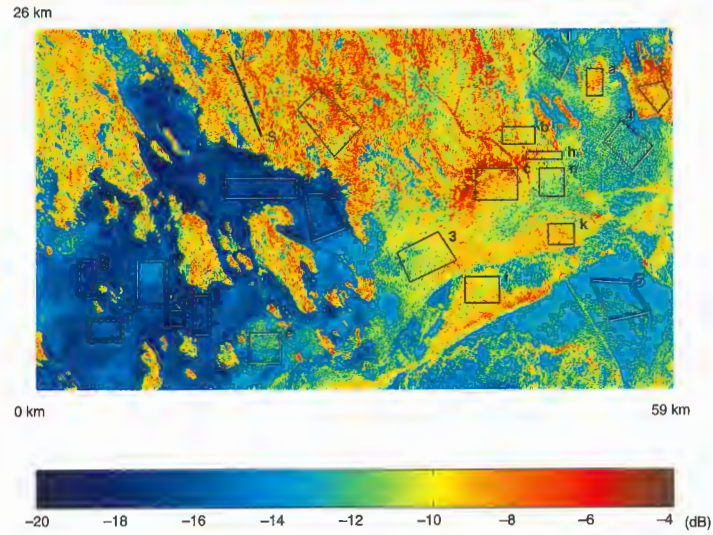
31

26 km

0 km   59 km

−20   −18   −16   −14   −12   −10   −8   −6   −4 (dB)

Figure 23: Calibrated low resolution image from 940326. The daily mean air temperature was -8^0C.

26 km

0 km   59 km
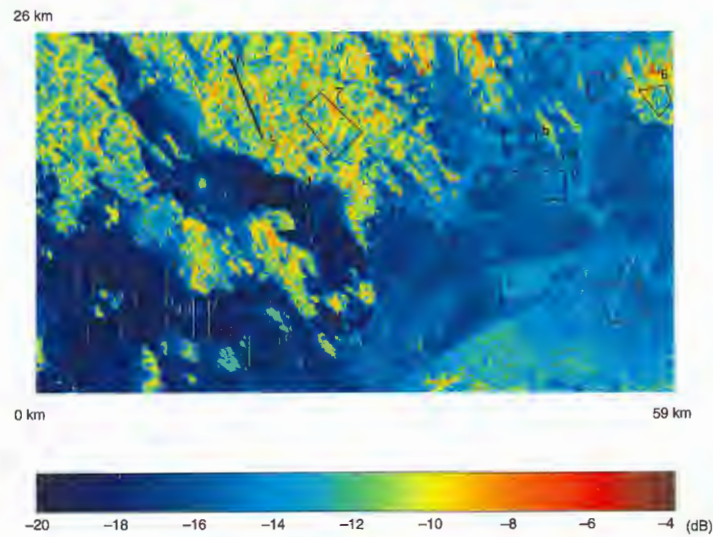
−20   −18   −16   −14   −12   −10   −8   −6   −4 (dB)

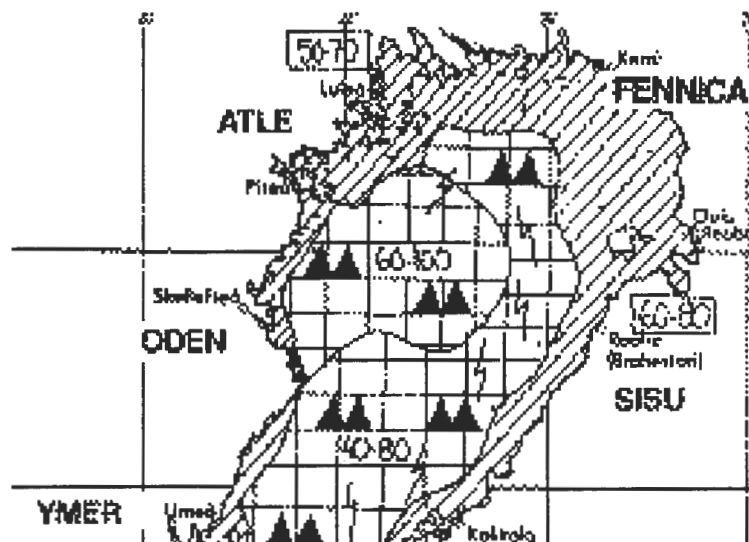Figure 24: Calibrated low resolution image from 940407. The daily mean air temperature was $+1^0C$.
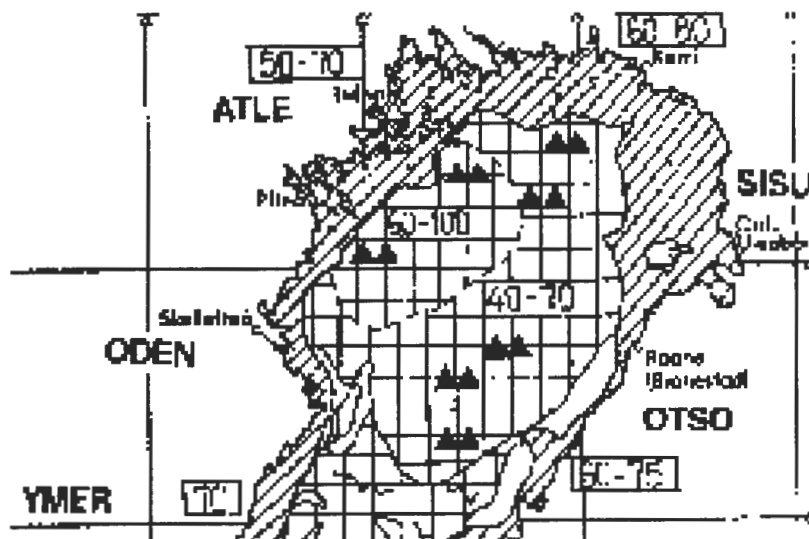
Figure 25: Ice chart from 940324.
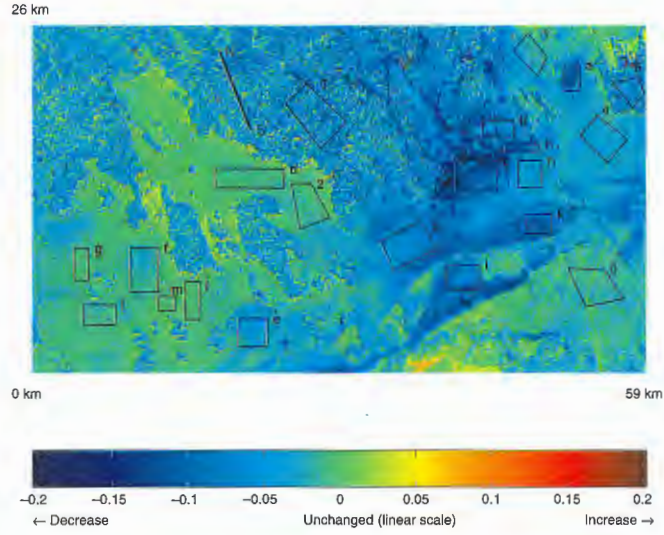

Figure 26: Ice chart from 940407.

33

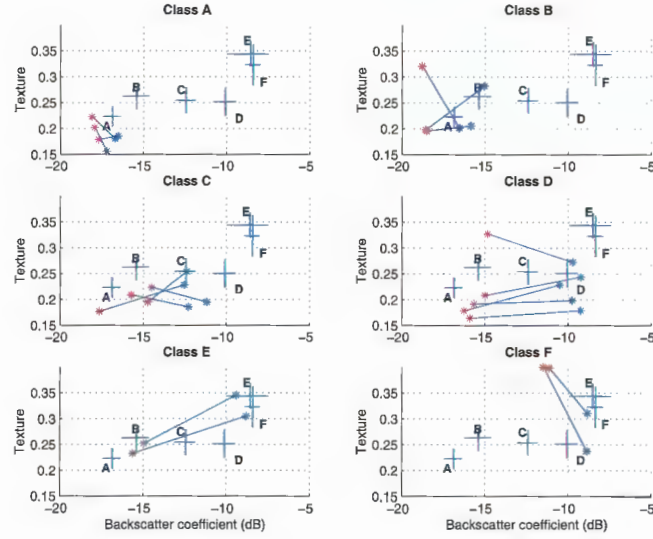Figure 27: Contrast in backscatter coefficient between the dates 940326 and 940407.

Figure 28: σ^0 and texture values of the six classes, as defined in Table 5. Blue stars mark the date 940326 and red stars mark the date 940407. Blue lines connect values from the same area.

34

In this section two images, recorded during different weather conditions, have been discussed. It has been shown that all areas decreased in backscatter when the air temperature rised. The reason is that wet snow absorbs the signal more effective than dry snow i.e. the surface looks smoother to the radar. The signal never reaches the rough ice underneath. High σ^0 values have decreased more than lower values. The rate of change in backscattering seems to depend on the type of surface class, while rate of change in texture varies within the classes. Number of discriminated ice classes decreases when air temperature rises.

8.5 Empirical Orthogonal Functions (EOF) Analysis

This section describes an Empirical Orthogonal Function (EOF) analysis of the image area. The section starts with a short discussion about the reasons of using EOFs.

An EOF analysis makes it possible to analyse the whole image area instead of studying homogeneous subareas, as in Section 8.1. Therefore, in order to study the dependency of ice texture and backscatter coefficient on weather parameters, an EOF analysis was carried out based on the entire data set. Since an EOF analysis filters out the dominating variations of the data set, weather dependent components can be separated from components influenced by other parameters.

To reduce the influence of speckle and to make the calculations faster, the images were averaged over 5×5 pixels. Due to the high demand of computer memory in the program used, the averaged scene was splitted into quarters according to Figure 29.

The eigenvalues representing more than 3% of the variance along the EOFs, are plotted in Figure 30. As indicated in the figure, the first EOF contains 45-60% of the energy in the fluctuation, while the second EOF contains less than 15% of the energy, except for the second EOF in area Q4 which keeps almost 25%. Area Q4 is probably affected by movements in the ice due to the short distance to the ice edge. This could influence the results since the study assumes stable ice conditions, i.e. the only changes in the ice occurs on the snow and ice surface.

Since the first EOF contains the main part of the energy in the fluctuations, it could be seen as a first approximation of the variations in the area, while the following EOFs are modifications/corrections of the first one [ECSW97].

The modal coefficients of the first EOF in each quarter, except in quarter Q4, show significant negative correlation ($> |0.60|$, see Section 8.1) with both the air temperature and water content of the air. The modal coefficients and the correlation coefficients of Q1-Q4 are shown in Figures 32, 34, 36 and 38, respectively. Only in a few cases the correlation coefficient differs between the two weather stations. In these cases, the highest correlation is specified. The modal coefficients in Q4 show only significant correlation with air water content.

The high correlation with the high energy modal coefficients, $a_1(t)$, may indicate that air temperature and air water content are the dominating parameters, affecting the backscatter value in the images. Air water content correlates on the same level or better than the temperature with the modal coefficients. There are of course other parameters affecting the backscatter but of less significance. Those may be found in lower energy modes, uncorrelated with air temperature and air water content. If for example there were two independent parameters dom-
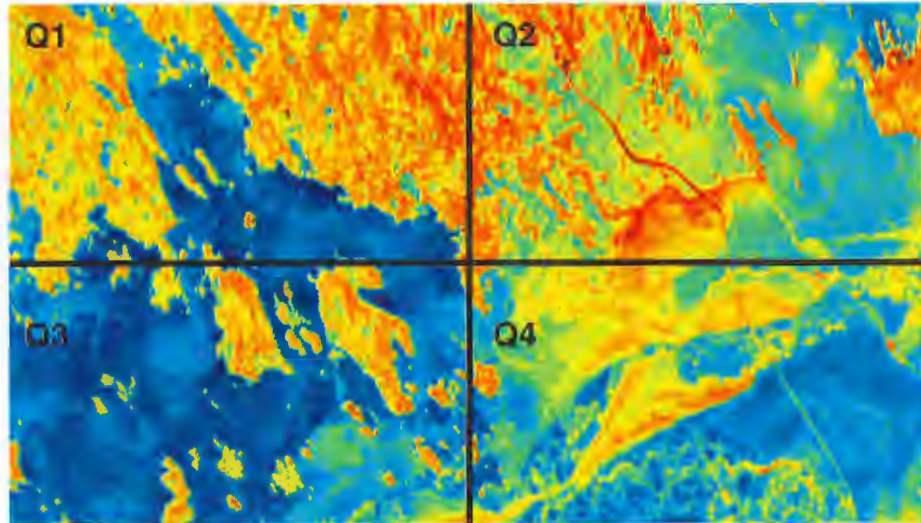
35

Figure 29: The division of the scene in the EOF calculation. The quarters are named Q1, Q2, Q3 and Q4 respectively.
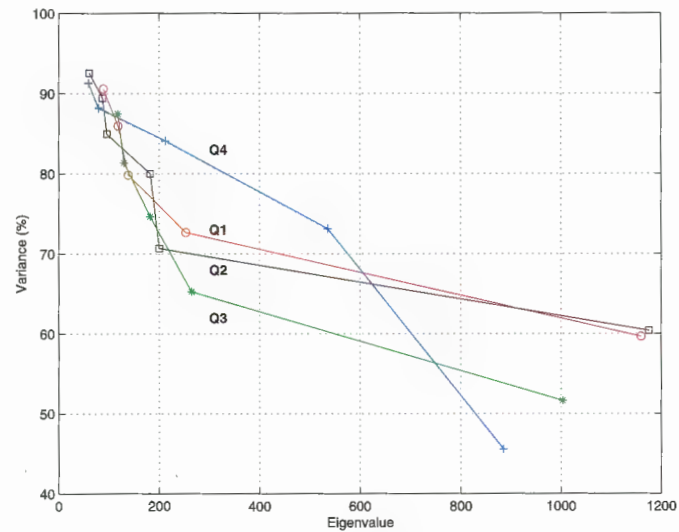

Figure 30: Eigenvalues representing more than 3% of the total variance derived from data in each quarter. The per cent is shown cumulative.

36

inating the backscattering process, there should be two EOFs of similar energy. This may be the case for the first two functions in quarter Q4, see Figure 30. The second EOF in area Q4 contains more energy compared to the second EOFs from the other areas in the image. Also it does not show any correlation with the weather parameters. This could mean that there is a parameter affecting the variations almost as much as the air water content. The second parameter involved could be movements in the ice due to wind or sea level changes.

Relative humidity and precipitation do not show any significant correlation with the modal functions. Since precipitation accumulates on the ground and changes properties due to wind and temperature, it is not sufficient to use momentary values. Instead the precipitation during a three day period was added. The changes of the snow cover due to wind and temperature were not taken into account.

The meaning of EOF values can be explained by the following statements:

I Similar pixel values of an EOF within an area means that the EOF has the same relation to all the pixels. The pixels follow each other in the variations.

II The absolute pixel value of the EOF describes how well the variation of the pixel follows the variation of the modal coefficient function, i.e. which area that dominates the variation of the EOF.

III Positive pixel values of an EOF means that the pixel value variation is in phase with the modal coefficient function, while negative values means that the variation is in opposite phase with the modal coefficient function.

In Sections 8.5.1 to 8.5.4 the four first EOFs and modal coefficients of each quarter are shown and described, to see how the variations are distributed within the image and how they physically could be explained. The roman figures in the following sections refer to the three statements above.

8.5.1   Area Q1

First EOF

Land and the central ice area show positive EOF values (I), see Figure 31, meaning that the pixel values follows the modal coefficient function variation (III). The modal coefficients of the first EOF show negative correlation with air temperature and air water content, see Figure 32 and Table 7. The negative correlation gives that σ^0 decreases with increasing temperature and air water content in the area. The EOF values are higher at land areas than at the central ice area. This means that the variation of the land pixel values are closer related than the variation of the central ice pixel values to the modal coefficient function variation (II).

Ice near the coastline has negative EOF pixel values, which means that the area varies in opposite phase to the modal coefficient function (III). This in combination with the negative correlation between the modal coefficient function and the weather parameters, gives that σ^0 increases with increasing temperature and air water content in the area.

Second EOF

The ice areas show positive values and land areas negative values (I). The second EOF does not show any significant correlation with any of the weather parameters.
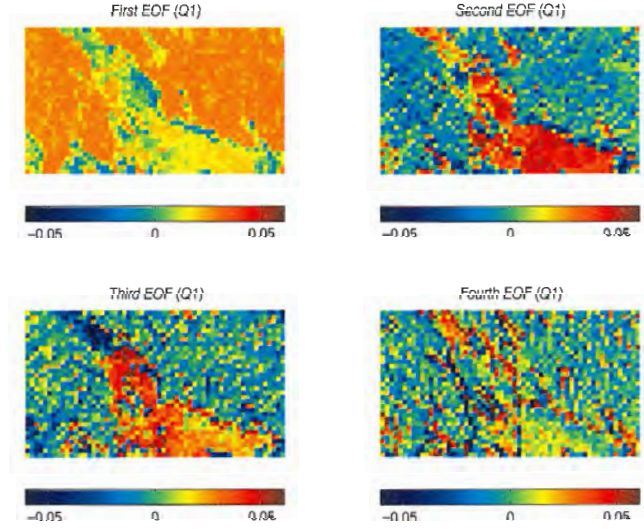
37

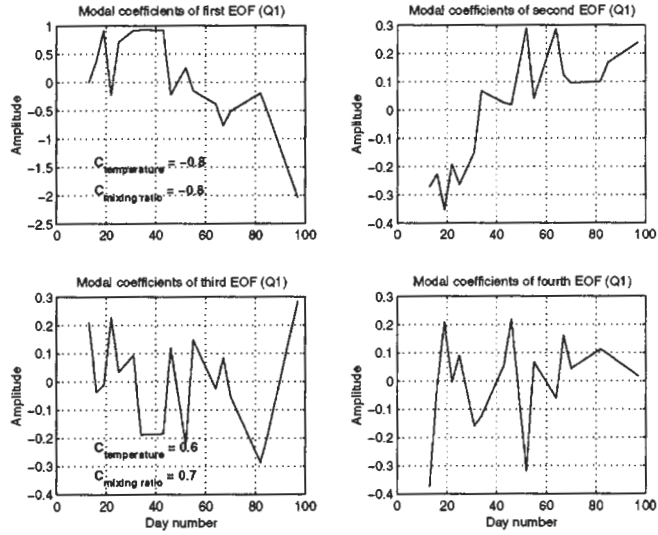Figure 31: The first four EOFs in area Q1.

Figure 32: The modal coefficient functions for the first four EOFs in area Q1. Only the significant correlation coefficients between the functions and weather parameters are shown.

Correlation coefficient	First EOF	Second EOF	Third EOF	Fourth EOF
Relative humidity (Fa)	-0.4998	0.1394	0.4558	-0.1464
Relative humidity (St)	-0.1235	0.1923	0.3796	-0.2855
Air temperature (Fa)	-0.8119	0.2295	0.6382	-0.0134
Air temperature (St)	-0.8608	0.3054	0.5259	0.0226
Air water content (Fa)	-0.8239	0.1847	0.7115	-0.0035
Air water content (St)	-0.8680	0.2533	0.6538	-0.0063

Table 7: The correlation coefficients between the weather parameters (daily means) and the modal coefficient functions for the first four EOFs in area Q1.

Third EOF

The pixel value distribution is similar to the distribution in the second EOF, except for very low values in the smooth ice area in the upper part of the image. The air temperature and air water content show positive correlation with the modal coefficients. The positive correlation gives that σ^0 follows the variations of air temperature and air water content in the ice areas (III), while the opposite is valid for land and the upper ice area. Compared to the results of the first EOF this may indicate that two counteracting processes affect the backscattering due to weather changes. Since the first EOF is the highest energy mode it contains the dominating process. On the other hand, the counteracting values may indicate that the variations in the first EOF were exaggerated and are compensated for by the third EOF.

Fourth EOF

The fourth EOF shows no correlation with the weather parameters and no specific area pattern (I).

8.5.2 Area Q2

First EOF

The entire area shows positive EOF values (I), see Figure 33, meaning that the pixel values follows the modal coefficient function variation (III). The modal coefficients show negative correlation with air temperature and air water content, see Figure 34 and Table 8. The negative correlation gives that σ^0 decreases with increasing temperature and air water content in the area.

The EOF values are slightly higher at ice areas than at land areas. This means that the variation of the ice pixel values are closer related than the variation of the land pixel values to the modal coefficient function (II). At Seskarö some EOF pixel values are negative.

Second EOF

The pixel values are negative at land areas (I). The ice areas in the right part of the image, including the very rough ice in the lower part, show positive values while ice in the archipelago shows high negative values (I). The second EOF does not show any significant correlation with any of the weather parameters.
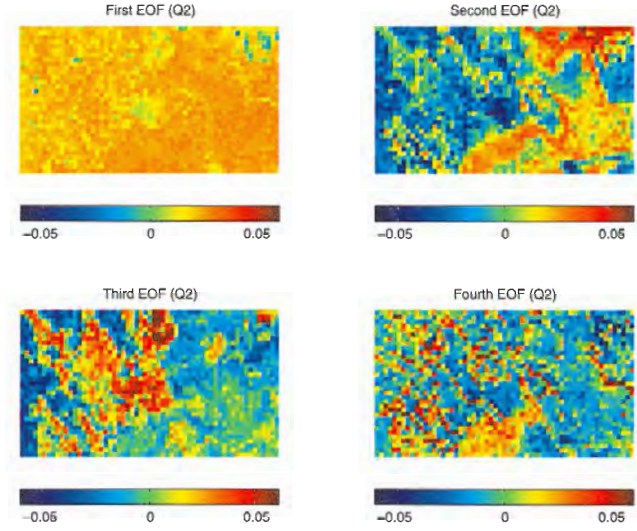
39

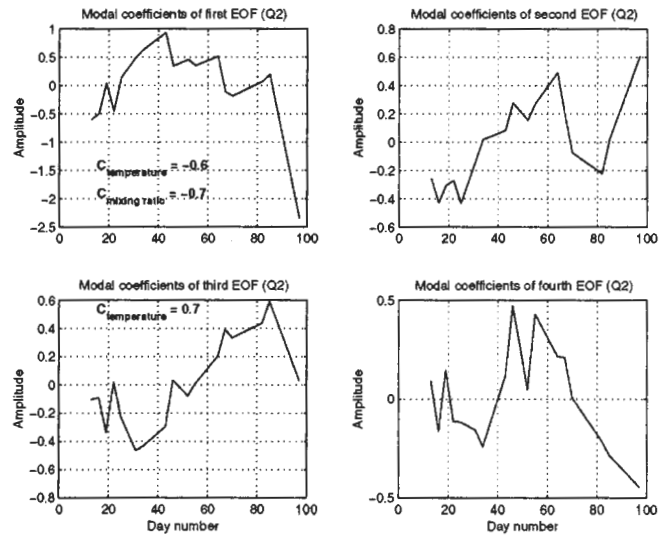Figure 33: The first four EOFs in area Q2.

Figure 34: The modal coefficient functions for the first four EOFs in area Q2. Only the significant correlation coefficients between the functions and weather parameters are shown.

40

Correlation coefficient	First EOF	Second EOF	Third EOF	Fourth EOF
Relative humidity (Fa)	-0.3977	0.2597	0.2964	0.2387
Relative humidity (St)	0.0209	0.4295	-0.1781	0.4527
Air temperature (Fa)	-0.6296	0.3573	0.5115	0.0533
Air temperature (St)	-0.6218	0.3630	0.6522	-0.0180
Air water content (Fa)	-0.7228	0.3712	0.4164	-0.0050
Air water content (St)	-0.7451	0.4084	0.4781	-0.1038

Table 8: The correlation coefficients between the weather parameters and the modal coefficient functions for the first four EOFs in area Q2.

Third EOF

The pixel values are negative at land areas. In opposite to the second EOF, the ice areas in the right part of the image shows negative values close to zero, while ice in the archipelago shows high positive values (I). It may indicate that two different processes affect the two different ice areas.

The modal coefficients correlate with the air temperature. The correlation is positive which means that the σ^0 values decrease with increasing air temperature at land areas, while σ^0 at ice areas in the archipelago increases with increasing air temperature. The more open ice areas, with values close to zero, have little relation with the modal coefficient function (III).

Fourth EOF

No specific area pattern is shown except for slightly higher values at the very rough ice in the lower part of the area (I). The fourth EOF shows no correlation with the weather parameters.

8.5.3   Area Q3

First EOF

The entire area shows positive EOF values (I), see Figure 35, meaning that the pixel values follows the modal coefficient function variation (III). The modal coefficients show negative correlation with air temperature and air water content, see Figure 36 and Table 9. The negative correlation gives that σ^0 decreases with increasing temperature and air water content in the area.

The EOF values are higher at open ice areas than at areas with islands. This means that the variation of the ice pixel values are closer related than the variation of the land pixel values to the modal coefficient function (II).

Second EOF

The ice areas show low positive values and the land areas high negative values (I). The modal coefficients show positive correlation with air temperature and air water content. The low values at the ice areas indicate little connection between the modal coefficient function and the EOF values of the ice areas (II), while the positive correlation and the negative land pixel val-
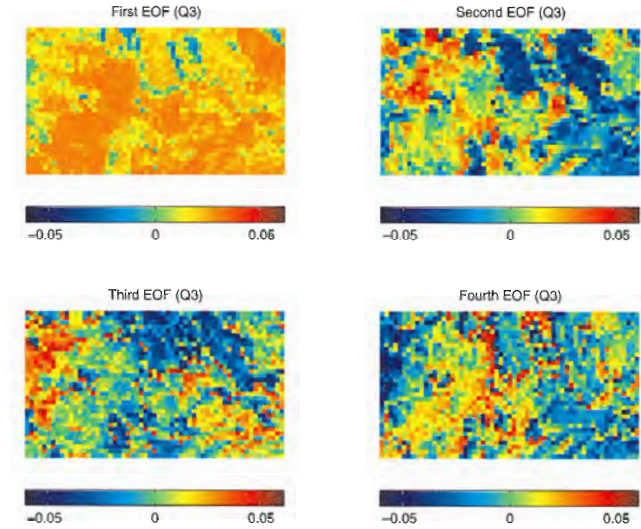
41

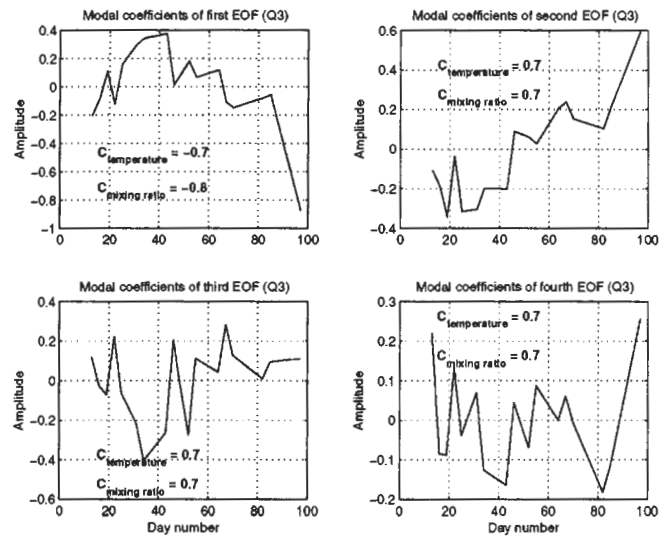Figure 35: The first four EOFs in area Q3.

Figure 36: The modal coefficient functions for the first four EOFs in area Q3. Only the significant correlation coefficients between the functions and weather parameters are shown.

Correlation coefficient	First EOF	Second EOF	Third EOF	Fourth EOF
Relative humidity (Fa)	-0.4499	0.4094	0.5016	0.5756
Relative humidity (St)	0.0013	0.1392	0.0622	0.4903
Air temperature (Fa)	-0.7463	0.6979	0.8015	0.7404
Air temperature (St)	-0.7602	0.7589	0.8191	0.6318
Air water content (Fa)	-0.8037	0.6921	0.7730	0.8038
Air water content (St)	-0.8272	0.7463	0.7513	0.7552

Table 9: The correlation coefficients between the weather parameters and the modal coefficient functions for the first four EOFs in area Q3.

ues give that σ^0 decreases with increasing temperature and air water content at land areas (III).

Third and Fourth EOF

The pixel value distribution is similar to the distribution in the second EOF. The air temperature and air water content show the same positive correlation with the modal coefficients as in the second EOF.

8.5.4   Area Q4

First EOF

Rough ice shows positive EOF values while less rough ice shows EOF values close to zero (I) in Figure 37. The modal coefficients of the first EOF show negative correlation with air water content, see Figure 38 and Table 10. The negative correlation gives that σ^0 decreases with increasing temperature and air water content in the rough ice area (III).

Second EOF

The second modal coefficient function shows no correlation with the weather parameters. As mentioned above, the high variance of the second EOF, see Figure 30, could be due to movements in the ice. It can be seen that the second EOF compensates the variations in the first EOF.

Third EOF and Fourth EOF

The modal coefficient functions of the third and fourth EOF in area Q4 show no correlation to the weather parameters. The line of high values in the third EOF may be due to displacement between the images in the time series or movements in the ice.

8.5.5   EOF Summary

A conclusion from the discussion above, is that the temperature and air water content are the dominating parameters affecting the backscattered signal in the image area. Land and ice areas do not respond in the same way in the EOFs and can therefore be distinguished from each other, while the differences between different ice classes are small in most cases. For example, in the EOFs that correlate with weather parameters, the very rough ice area in Q2 does not differ from the smoother ice. The differences that can be seen in area Q4 is probably
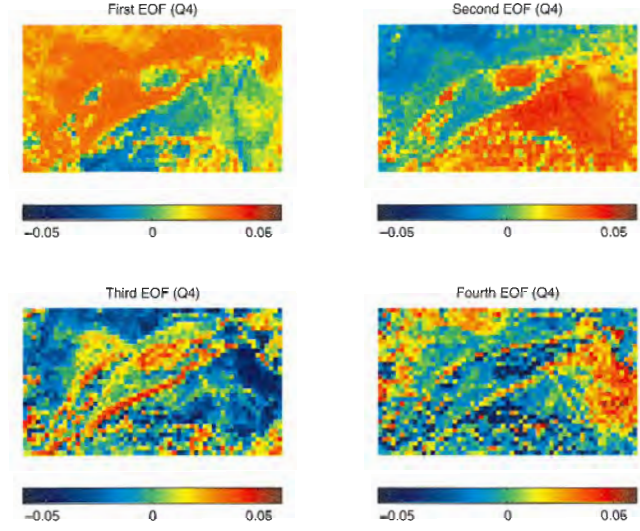
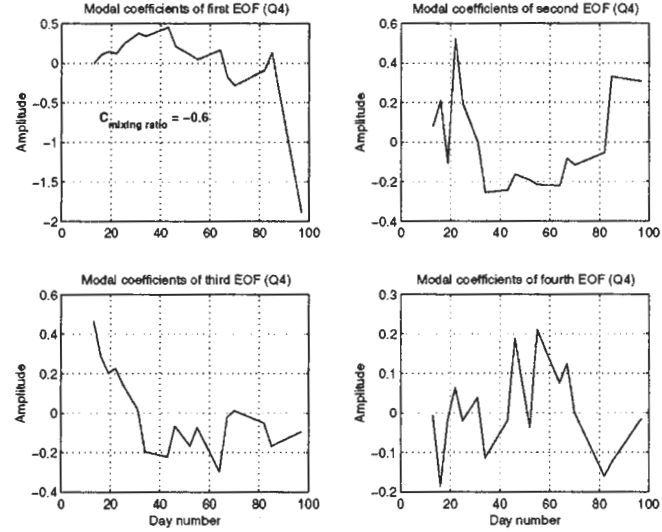Figure 37: The first four EOFs in area Q4.

Figure 38: The modal coefficient functions for the first four EOFs in area Q4. Only the significant correlation coefficients between the functions and weather parameters are shown.

44

Correlation coefficient	First EOF	Second EOF	Third EOF	Fourth EOF
Relative humidity (Fa)	-0.4339	-0.0499	0.2009	0.3912
Relative humidity (St)	-0.1412	-0.4854	-0.1021	0.6265
Air temperature (Fa)	-0.5602	0.4564	0.1819	0.3962
Air temperature (St)	-0.5591	0.5288	0.1150	0.2736
Air water content (Fa)	-0.6528	0.4768	0.2106	0.3950
Air water content (St)	-0.6874	0.5444	0.1389	0.3011

Table 10: The correlation coefficients between the weather parameters and the modal coefficient functions for the first four EOFs in area Q4.

due to movements in the ice and not different ice classes.

The first and third EOFs generally indicate that there are two counteracting processes affecting the backscatter coefficient of ice due to weather changes. The dominating process (in the first EOFs) decreases σ^0 with increasing temperature and air water content, while the lower energy mode (the third EOFs) indicates a process where σ^0 increases with increasing temperature and air water content. On the other hand the counteracting values may indicate that the variations in the first EOF were exaggerated and are compensated for by the third EOF.

On land, both the first and third EOFs, implies that the backscatter coefficient decreases for increasing temperature.

9 Summary and Conclusion

In this thesis the dependency of texture and backscatter of ice in LRI images, on air temperature, air humidity, air water content and precipitation has been described.

Six surface classes in the LRI have been defined. One land class and five ice classes, including two classes of deformed ice and three level ice classes. It has been shown that smooth ice differs from rough ice only in σ^0, while very rough ice differs from all other ice classes in all the three categories; temporal variability, texture and backscatter coefficient. Land and very rough ice only differ in temporal variability. A reason for the differences in temporal variability between rough ice and land could be due to the differences in temperature gradient in their "bottom layers". The sea below the ice has a temperature of zero degrees centigrade, while the frozen land has a temperature far below zero. This implies that the snow cover on land keeps a relatively constant humidity even if the air temperature varies. The humidity of the snow on the ice on the other hand, is affected by the heat source from below and are therefore more sensitive to an increase in air temperature. Since rough ice has higher backscatter values, it varies within a larger interval than smoother ice. The discussion above should be valid for comparisons between all ice classes, but according to Figure 21 there is a discontinuity between rough and less rough ice.

In comparison to a classification of contemporary FD images, the LRI backscatter coefficients are on average higher.

In a case study, two images recorded during

different weather conditions have been discussed. It has been shown that all the 21 areas that represent the different surface classes, decreased in backscatter when the air temperature rised above zero. The reason is that wet snow scatters and at the same time absorbs the signal more effective compared to dry snow, i.e. the surface looks smoother since the ice underneath is less visible to the radar. High σ^0 values have decreased more than lower values. The rate of change in backscattering seems to depend on surface class, while rate of change in texture varies within the class.

In the study of the variability of mean backscatter coefficient of separated homogeneous areas, the land areas correlate with air temperature and air water content. However, four ice areas, mainly within deformed ice (class $\mathbf{D}$), correlate with air water content.

The whole image area, was analysed with EOFs. As a result of the EOF analysis, the temperature and air water content are the dominating parameters affecting the backscattered signal in the image area. Land and ice areas do not respond in the same way in the EOFs and can therefore be distinguished from each other, while the differences between different ice classes are small in most cases. The analysis also indicates that there are two counteracting processes affecting the backscatter coefficient of ice due to weather changes. Since the EOFs only are statistically related, the two counteracting processes could be an effect of the definitions of the EOFs. The dominating process decreases σ^0 with increasing temperature and air water content, while the less dominating process indicates that σ^0 increases with increasing temperature and air water content. The first process mentioned describes the same process that decreases the backscatter coefficient in the case study de-

scribed above. The latter, less dominant process, could be an increased snow grain size due to higher temperature and air water content. This increases the backscatter coefficient.

The land area differs from ice areas also in the EOF analysis, which could be explained by the difference in temperature gradients described above.

10 Future Work

It is important to further develop the interpretation of SAR images and increase the understanding of the effects of various weather conditions. In order to achieve higher accuracy in the practical use of SAR images, for example in the ice breaking services, it is necessary to more precisely determine the ice backscatter coefficient for different weather situations.

Firstly the influence of wet snow must be further investigated. This can be achieved by using more frequent and longer time series of SAR images from periods with large variations in weather conditions. RADARSAT SAR images can be received every second day and could therefore be used for this purpose. The problem with RADARSAT is to compare data from different incidence angles due to the wide swath.

Secondly, the influence of wind on the ice backscatter coefficient has not been investigated here. The wind affects the snow and ice surface roughness and is therefore an important parameter when determining the ice backscatter coefficient for different weather conditions. More momentary in situ measurements of the weather parameters would decrease the number of errors depending on local weather changes. In this study, only data from two weather stations were available. Since the backscatter coefficient varies a

lot in the temperatures around zero degrees, another improvement would be to use correlation methods that trace nonlinear relations. Also it would be useful to take into account time shifts between variables.

Thirdly, in order to understand the differences in backscatter between land and ice surfaces, their humidity and temperature gradients should be investigated.

Finally, a further investigation of the standard deviation image should be carried out. As an extra feature, it is also possible to produce a land mask using Equation 21.

In the future, the unique collection of instruments on board Envisat-1 (see Section 2.4), will record data sets consisting of large amounts of parameters. This will develop our understanding within Earth science and the large number of parameters recorded, will also increase the understanding of many features of the measured data.

11   Acknowledgements

References

[Car94]   A. Carlström. Baltic experiment for ERS-1, BEERS-94 data report. Technical Report Internal Report RSG 1994:2, Department of Radio and Space Science at Chalmers University of Technology, Aug 1994.

[Car95]   A. Carlström. *Modelling Microwave Backscattering from Sea Ice for Synthetic-Aperture Radar Applications.* PhD thesis, Department of Radio and Space Science at Chalmers University of Technology, 1995.

[Dam93]   P. Dammert. Radarsignaturer av havsis i bottenviken. Master's thesis, Department of Radio and Space Science at Chalmers University of Technology, 1993.

[DUL94]   P. Dammert, L. Ulander, and B. Larsson. E: ERS-1 SAR signatures of sea ice and leads. Winter Navigation Research Board Research Report 51:Baltic Experiment for ERS-1 (BEERS), Finnish Board of Navigation and National Maritime Administration Sweden, Dec 1994.

[ECSW97]   R. Everson, P. Cornillon, L. Sirovich, and A. Webber. An empirical eigenfunction analysis of sea surface temperatures in the western north atlantic. *Journal of Physical Oceanography*, 27:468–479, 1997.

[Ela88]   C. Elachi. *Spaceborne Radar Remote Sensing:Applications and Techniques.* IEEE PRESS, 1988.

[ET98]   W.J. Emery and R.E. Thomson. *Data Analysis Methodes in Physical Oceanography.* Pergamon, 1998.

[Fre92]   A. Freeman. SAR calibration: An overview. *IEEE Transactions on Geoscience and Remote Sensing*, 30:1107–1121, 1992.

[HH95]   D.R. Helsel and R.M. Hirsch. *Statistical Methods in Water Resources.* ELSEVIER, 1995.

[IRS93]   E. Ingelstam, R. Rönngren, and S. Sjöberg. *TEFYMA Handbok för grundläggande teknisk fysik, fysik och matematik.* Sjöbergs bokförlag AB, 1993.

[Jol90]   I.T. Jolliffe. Principal component analysis: A beginner's guide - 1. Introduction and application. *Weather*, 45(10):375–382, 1990.

[LBM⁺98]   H. Laur, P. Bally, P. Meadows, J. Sanchez, B. Schaettler, E. Lopinto, and D. Esteban. ERS-1 SAR calibration: Derivation of the backscattering coefficient σ_0 in ESA ERS SAR PRI products. Document Issue 2.5, ESA, June 1998.

[LDKM95] B. Landmark, Ø.B. Dick, K. Kloster, and J. Moen. Earth observation, 1995.

[MH94] M. Moberg and B. Håkansson. F: Influence of temperature and precipitation during cold conditions on ERS-1 SAR sea ice imegary. Winter Navigation Research Board Research Report 51:Baltic Experiment for ERS-1 (BEERS), Finnish Board of Navigation and National Maritime Administration Sweden, Dec 1994.

[MPAH97] S. Mugnier-Pollet, J. Askne, and B. Håkansson. Retrival of sea surface wind speed from ERS-1/2 SAR. In *CEOS Wind and Wave Validation Workshop; Symposium held in Noordwijk Norway*, number 147 in WPP (ESA), pages 209–214, 1997.

[Pre88] R.W. Preisendorfer. *Principal Component Analysis in Meteorology and Oceanography.* Elsevier, 1988.

[RJ96] R. Reyment and K.G. Jöreskog. *Applied Factor Analysis in the Natural Sciences.* Cambridge University Press, 1996.

[Rob95] I.S. Robinson. *Satellite Oceanography: An introduction for Oceanographers and Remote-Sensing Scientists.* John Wiley & Sons, 1995.

[UJA92] L.M.H. Ulander, R. Johansson, and J. Askne. C-band radar backscatter of baltic sea ice: Theoretical predictions compared with calibrated SAR measurements. *International Jornal of Remote Sensing*, 13:2447–2468, 1992.

[Ula94] L.M.H. Ulander. B: Description and calibration of ERS-1 SAR images. Winter Navigation Research Board Research Report 51: Baltic Experiment for ERS-1 (BEERS), Finnish Board of Navigation and National Maritime Administration Sweden, Dec 1994.

[Ula97] 1997. Personal communication with Lars M.H. Ulander, FOA, Linköping, Sweden.

[WH77] J.M. Wallace and P.V. Hobbs. *Atmospheric Science: An introductory survey.* Academic Press, Inc, 1977.
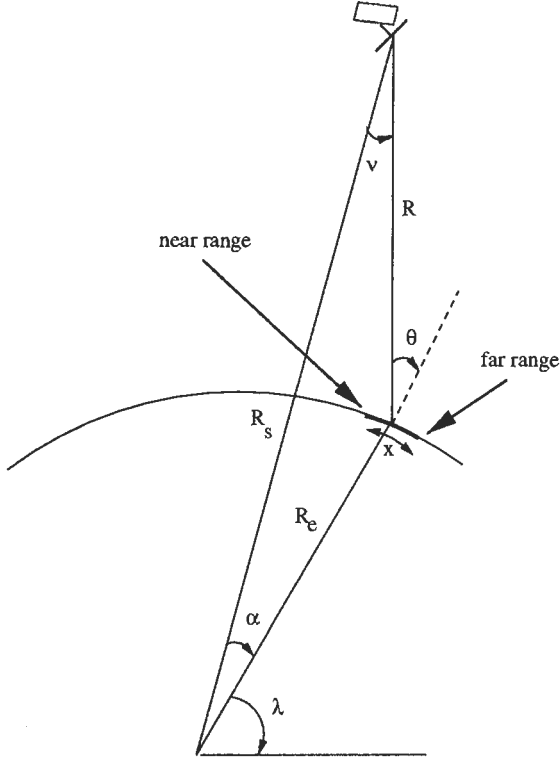
A   Calculation of R, θ and ν

Figure 39: Geometry of ERS-1 SAR. R is the distance between satellite and target. θ is the incidence angle. ν is the antenna elevation angle, also called look angle. Due to the curvature of earth surface $\theta > \nu$.

In this appendix R, θ and ν in Figure 39 will be calculated step by step across the swath. R, θ and ν are used in the calculate of the range correction, f in Equation 11.

R_1, distance between satellite and near edge

To calculate the distance between satellite and near edge, R_1, the *zero Doppler range time*, t_1, given by the LRI header is used. *Zero Doppler range time)* is the time it takes for the signal to travel from the satellite to near edge and back.

$$R_1 = c\frac{t_1}{2} \qquad (22)$$

where c is the light velocity. $t_1 = 5.54 \cdot 10^{-3}$ s gives $R_1 = 830690$ m.

R_e, Earth radius

The latitude $\lambda = 66°$ and the GEM-6 ellipsoid model, gives the Earth radius $R_e = 6360352$ m by following equation:

$$R_e = a\sqrt{\frac{\cos^2\lambda + (b/a)^4 sin^2\lambda}{\cos^2\lambda + (b/a)^2 sin^2\lambda}} \qquad (23)$$

where a and b represent the equatorial and the polar Earth radius respectively. $a = 6378.17$ km and $b = 6356.79$ km [IRS93].

R_s, satellite radius

The near edge information of incidence angle is not accessible neither in the FD or in the LRI header. According to [Ula94] a good assumption of the incidence angle at near edge, θ_1, is $19.4°$. R_1, R_e and θ_1 and the law of cosine give the satellite radius, R_s, see Figure 39.

$$R_s = \sqrt{R_1^2 + R_e^2 - 2R_1R_e\cos(\pi - \theta_1)} \qquad (24)$$

ν_1, look angle at near edge

The look angle at near edge, ν_1, is derived from R_e, R_s and θ_1 and the law of sine.

$$\frac{\sin\nu_1}{R_e} = \frac{\sin(\pi - \theta_1)}{R_s}$$
$$\Longrightarrow$$
$$\nu_1 = \arcsin(R_e\frac{\sin(\pi - \theta_1)}{R_s}) \qquad (25)$$

50

α_1 - near edge

θ_1 and ν_1 give α_1.

$$\alpha_1 = \pi - \nu_1 - (\pi - \theta_1) = \theta_1 - \nu_1 \qquad (26)$$

Calculations over the entire swath

At this point, all parameters at near edge, R_1, θ_1, ν_1 and α_1, are known, including R_e and R_s. To go further there are two possible assumptions to choose between. The first possibility is to assume $\theta = 23^\circ$ in the middle of the image. The second possibility is to assume that the swath represents an arc of 100 km and 50 km at mid range. The last alternative is chosen, since it has shown best result in previous calculation according to [Ula97]. The difference between the alternatives is not big. 50 km at mid range gives $\theta = 26.5^\circ$ at far range while $\theta = 23^\circ$ at mid range gives 26.6° at far range. The deviation from the true angles is maximum ± 0.2 ° [Ula94].

The angle α

Assuming the arc, x varies over the swath gives

$$\alpha = \alpha_1 + \frac{x}{R_e} \qquad (27)$$

where α_1 is given in radians.

R, slant range

R, the slant range is received from α and the law of cosine.

$$R = \sqrt{R_e^2 + R_s^2 - 2R_e R_s \cos \alpha} \qquad (28)$$

ν, look angle

ν, the look angle can be calculated from R_e, R and α and the law of sine, Equation 25

$$\frac{\sin \nu}{R_e} = \frac{\sin \alpha}{R}$$
$$\Longrightarrow$$
$$\nu_1 = \arcsin(R_e \frac{\sin \alpha}{R}) \qquad (29)$$

θ, incidence angle

The incidence angle θ across the image is given by

$$\pi = \nu + \alpha + (\pi - \theta)$$
$$\Longrightarrow$$
$$\theta = \nu + \alpha \qquad (30)$$

The parameters R, θ and ν is now known for each pixel across the swath and can be used in the calculation of the range correction, f in Equation 11.

B   Glossary - Ice Classes

Level ice - Slät is
Deformed ice - Deformerad is
Ridged ice - Is med vallar
Hummocked ice - Upptornad is
Jammed brash barrier -
*   Is i form av en stampvall*

C   Correlation Coefficients

Class	Area	Rel. hum. (Fa)/(St)	Air temp. (Fa)/(St)	Air water cont. (Fa)/(St)
A	g	-0.1240/0.0259	-0.0618/-0.0019	-0.1296/-0.0358
	j	-0.2683/0.0970	-0.4382/-0.4367	-0.4686/-0.4489
	m	-0.2822/0.0378	-0.3635/-0.3783	-0.3968/-0.3717
B	d	-0.2238/0.1964	-0.4423/-0.4772	-0.4651/-0.4634
	f	-0.2103/0.2293	-0.4732/-0.5261	-0.5278/-0.5437
	l	-0.1979/0.2392	-0.4821/-0.5393	-0.5080/-0.5305
C	1	-0.3404/0.0829	-0.4496/-0.4689	-0.5177/-0.4938
	4	-0.4386/-0.0370	-0.4640/-0.4678	-0.5502/-0.5227
	e	-0.2909/0.0024	-0.4551/-0.4855	-0.5358/-0.6048
	n	-0.4401/-0.1052	-0.3880/-0.3733	-0.5008/-0.4769
D	3	-0.3303/0.0193	-0.5547/-0.5965	-0.6162/-0.6871
	a	-0.3395/-0.0073	-0.4488/-0.4726	-0.5497/-0.5678
	b	-0.3364/-0.3218	-0.1539/-0.1464	-0.3162/-0.3556
	i	-0.3397/-0.0366	-0.5279/-0.5684	-0.5953/-0.6737
	k	-0.3627/-0.0758	-0.5322/-0.5685	-0.6048/-0.6825
E	c	-0.1263/0.2656	-0.3530/-0.3585	-0.4001/-0.3811
	h	-0.1191/0.2681	-0.3086/-0.3165	-0.3559/-0.3328
F	6	-0.3728/0.0502	-0.7093/-0.7643	-0.7543/-0.8188
	7	-0.3443/0.0567	-0.7962/-0.8503	-0.791/-0.8665

Table 11: The correlation coefficients between the weather parameters (daily means) and the mean backscatter coefficients of the areas marked in Figure 18. Fa = Farstugrunden, St = Storöhamn. The capital letters, (A − F) refer to the surface classes in Table 5. Areas 2 and 5 are excluded since their areas are not homogeneous and probably contain more than one ice class.

SMHIs publications

SMHI publishes six report series. Three of these, the R-series, are intended for international readers and are in most cases written in English. For the others the Swedish language is used.

Names of the Series	Published since
RMK (Report Meteorology och Climatology)	1974
RH (Report Hydrology)	1990
RO (Report Oceanography)	1986
METEOROLOGI	1985
HYDROLOGI	1985
OCEANOGRAFI	1985

Earlier issues published in serie RO

1 Lars Gidhagen, Lennart Funkquist and Ray Murthy (1986)
Calculations of horizontal exchange coefficients using Eulerian time series current meter data from the Baltic Sea.

2 Thomas Thompson (1986)
Ymer-80, satellites, arctic sea ice and weather.

3 Stig Carlberg et al (1986)
Program för miljökvalitetsövervakning - PMK.

4 Jan-Erik Lundqvist och Anders Omstedt (1987)
Isförhållandena i Sveriges södra och västra farvatten.

5 Stig Carlberg, Sven Engström, Stig Fonselius, Håkan Palmén, Eva-Gun Thelén, Lotta Fyrberg och Bengt Yhlen (1987)
Program för miljökvalitetsövervakning - PMK. Utsjöprogram under 1986.

6 Jorge C. Valderama (1987)
Results of a five year survey of the distribution of UREA in the Baltic sea.

7 Stig Carlberg, Sven Engström, Stig Fonselius, Håkan Palmén, Eva-Gun Thelén, Lotta Fyrberg, Bengt Yhlen och Danuta Zagradkin (1988).
Program för miljökvalitetsövervakning - PMK. Utsjöprogram under 1987.

8 Bertil Håkansson (1988)
Ice reconnaissance and forecasts in Storfjorden, Svalbard.

9 Stig Carlberg, Sven Engström, Stig Fonselius, Håkan Palmén, Eva-Gun Thelén, Lotta Fyrberg, Bengt Yhlen, Danuta Zagradkin, Bo Juhlin och Jan Szaron (1989)
Program för miljökvalitetsövervakning - PMK. Utsjöprogram under 1988.

10 L. Fransson, B. Håkansson, A. Omstedt och L. Stehn (1989)
Sea ice properties studied from the icebreaker Tor during BEPERS-88.

11 Stig Carlberg, Sven Engström, Stig Fonselius, Håkan Palmén, Lotta Fyrberg, Bengt Yhlen, Bo Juhlin och Jan Szaron (1990)
Program för miljökvalitetsövervakning - PMK. Utsjöprogram under 1989.

12 Anders Omstedt (1990)
Real-time modelling and forecasting of temperatures in the Baltic Sea.

13 Lars Andersson, Stig Carlberg, Elisabet Fogelqvist, Stig Fonselius, Håkan Palmén, Eva-Gun Thelén, Lotta Fyrberg, Bengt Yhlen och Danuta Zagradkin (1991)
Program för miljökvalitetsövervakning - PMK. Utsjöprogram under 1990.

14   Lars Andersson, Stig Carlberg, Lars Edler, Elisabet Fogelqvist, Stig Fonselius, Lotta Fyrberg, Marie Larsson, Håkan Palmén, Björn Sjöberg, Danuta Zagradkin, och Bengt Yhlen (1992)
Haven runt Sverige 1991. Rapport från SMHI, Oceanografiska Laboratoriet, inklusive PMK - utsjöprogrammet. (The conditions of the seas around Sweden. Report from the activities in 1991, including PMK - The National Swedish Programme for Monitoring of Environmental Quality Open Sea Programme.)

15   Ray Murthy, Bertil Håkansson and Pekka Alenius (ed.) (1993)
The Gulf of Bothnia Year-1991 - Physical transport experiments.

16   Lars Andersson, Lars Edler and Björn Sjöberg (1993)
The conditions of the seas around Sweden. Report from activities in 1992.

17   Anders Omstedt, Leif Nyberg and Matti Leppäranta (1994)
A coupled ice-ocean model supporting winter navigation in the Baltic Sea.
Part 1. Ice dynamics and water levels.

18   Lennart Funkquist (1993)
An operational Baltic Sea circulation model. Part 1. Barotropic version.

19   Eleonor Marmefelt (1994)
Currents in the Gulf of Bothnia. During the Field Year of 1991.

20   Lars Andersson, Björn Sjöberg and Mikaell Krysell (1994)
The conditions of the seas around Sweden. Report from the activities in 1993.

21   Anders Omstedt and Leif Nyberg (1995)
A coupled ice-ocean model supporting winter navigation in the Baltic Sea.
Part 2. Thermodynamics and meteorological coupling.

22   Lennart Funkquist and Eckhard Kleine (1995)
Application of the BSH model to Kattegat and Skagerrak.

23   Tarmo Köuts and Bertil Håkansson (1995)
Observations of water exchange, currents, sea levels and nutrients in the Gulf of Riga.

24   Urban Svensson (1998)
PROBE An Instruction Manual.

SMHI